E9863-3
7/31/98

NASA/TM—1998-107249/CH3

Solid Lubrication Fundamentals and Applications

Properties of Clean Surfaces: Adhesion, Friction, and Wear

Kazuhisa Miyoshi
Lewis Research Center, Cleveland, Ohio

July 1998

The NASA STI Program Office . . . in Profile

Since its founding, NASA has been dedicated to the advancement of aeronautics and space science. The NASA Scientific and Technical Information (STI) Program Office plays a key part in helping NASA maintain this important role.

The NASA STI Program Office is operated by Langley Research Center, the Lead Center for NASA's scientific and technical information. The NASA STI Program Office provides access to the NASA STI Database, the largest collection of aeronautical and space science STI in the world. The Program Office is also NASA's institutional mechanism for disseminating the results of its research and development activities. These results are published by NASA in the NASA STI Report Series, which includes the following report types:

- TECHNICAL PUBLICATION. Reports of completed research or a major significant phase of research that present the results of NASA programs and include extensive data or theoretical analysis. Includes compilations of significant scientific and technical data and information deemed to be of continuing reference value. NASA's counterpart of peer-reviewed formal professional papers but has less stringent limitations on manuscript length and extent of graphic presentations.

- TECHNICAL MEMORANDUM. Scientific and technical findings that are preliminary or of specialized interest, e.g., quick release reports, working papers, and bibliographies that contain minimal annotation. Does not contain extensive analysis.

- CONTRACTOR REPORT. Scientific and technical findings by NASA-sponsored contractors and grantees.

- CONFERENCE PUBLICATION. Collected papers from scientific and technical conferences, symposia, seminars, or other meetings sponsored or cosponsored by NASA.

- SPECIAL PUBLICATION. Scientific, technical, or historical information from NASA programs, projects, and missions, often concerned with subjects having substantial public interest.

- TECHNICAL TRANSLATION. English-language translations of foreign scientific and technical material pertinent to NASA's mission.

Specialized services that complement the STI Program Office's diverse offerings include creating custom thesauri, building customized data bases, organizing and publishing research results . . . even providing videos.

For more information about the NASA STI Program Office, see the following:

- Access the NASA STI Program Home Page at ***http://www.sti.nasa.gov***

- E-mail your question via the Internet to help@sti.nasa.gov

- Fax your question to the NASA Access Help Desk at (301) 621-0134

- Telephone the NASA Access Help Desk at (301) 621-0390

- Write to:
  NASA Access Help Desk
  NASA Center for AeroSpace Information
  800 Elkridge Landing Road
  Linthicum Heights, MD 21090-2934

NASA/TM—1998-107249/CH3

Solid Lubrication Fundamentals and Applications

Properties of Clean Surfaces: Adhesion, Friction, and Wear

Kazuhisa Miyoshi
Lewis Research Center, Cleveland, Ohio

National Aeronautics and
Space Administration

Lewis Research Center

July 1998

Available from

NASA Center for Aerospace Information
800 Elkridge Landing Road
Linthicum Heights, MD 21090-2934
Price Code: A04

National Technical Information Service
5287 Port Royal Road
Springfield, VA 22100
Price Code: A04

Chapter 3
Properties of Clean Surfaces: Adhesion, Friction, and Wear

3.1 Introduction and Approach

As described in Chapter 2, a contaminant layer may form on a solid surface either by the surface interacting with the environment or by the bulk contaminant diffusing through the solid itself. Thin contaminant layers, such as adsorbed gases, water vapor, and hydrocarbons of atomic dimensions (approximately 2 nm thick), are unavoidably present on every surface of any solid that has been exposed to air. Surface analysis techniques, particularly x-ray photoelectron spectroscopy (XPS) and Auger electron spectroscopy (AES), are well suited for examining these thin contaminant layers. However, contaminant surface layers can affect the spectrum by attenuating the electron signal from the underlying surface, thereby masking spectral features related to the bulk material [3.1–3.3].

Contamination is an important factor in determining such solid surface properties as adhesion and friction. Contaminant layers can greatly reduce adhesion and friction and, accordingly, provide lubrication. The adhesion, friction, and wear behaviors of contaminated surfaces will be discussed in Chapter 4.

Because contaminants are weakly bound to the surface, physically rather than chemically, they can be removed by bombarding them with rare gas ions (e.g., argon ions) or by heating to say 700 °C [3.4, 3.5]. Contaminant surface layers can also be removed by repeated sliding, making direct contact of the fresh, clean surfaces unavoidable [3.3, 3.6]. This situation applies in some degree to contacts sliding in air, where fresh surfaces are continuously produced by a counterfacing material. It also applies in vacuum tribology to wear-resistant components used in aerospace mechanisms, semiconductor-processing equipment, machine tool spindles, etc. Obviously, understanding the behavior of clean surfaces in metal-ceramic couples is of paramount practical importance.

This chapter presents the fundamental tribology of clean surfaces (i.e., the adhesion, friction, and wear behaviors of smooth, atomically clean surfaces of solid-solid couples, such as metal-ceramic couples, in a clean environment). Surface and bulk properties, which determine these behaviors, are described. The primary emphasis is on the nature and character of the metal, especially its surface energy and ductility. Also, the friction and wear mechanisms of clean, smooth surfaces are stated.

To understand the adhesion and friction behaviors of atomically clean solid surfaces, a simple experimental approach has been taken to control and characterize as carefully as possible the materials and environment in tribological studies [3.1, 3.4, 3.7–3.11]. High-purity metals are used, as much as possible, in an ultrahigh vacuum (Fig. 3.1) that contains an XPS or AES spectrometer [3.7–3.11]. Adsorbed contaminant layers (water vapor, carbon monoxide and dioxide, hydrocarbons, and oxide layers) are removed by argon sputtering. Surface cleanliness is verified by AES or XPS (see Chapter 2). Adhesion and friction are measured by a pin-on-flat configuration, as shown in Fig. 3.1. Removing contaminant films from the surfaces of solids has enabled us to better understand the surface and bulk properties that influence adhesion and friction when two such solids are brought into contact in an ultrahigh vacuum.

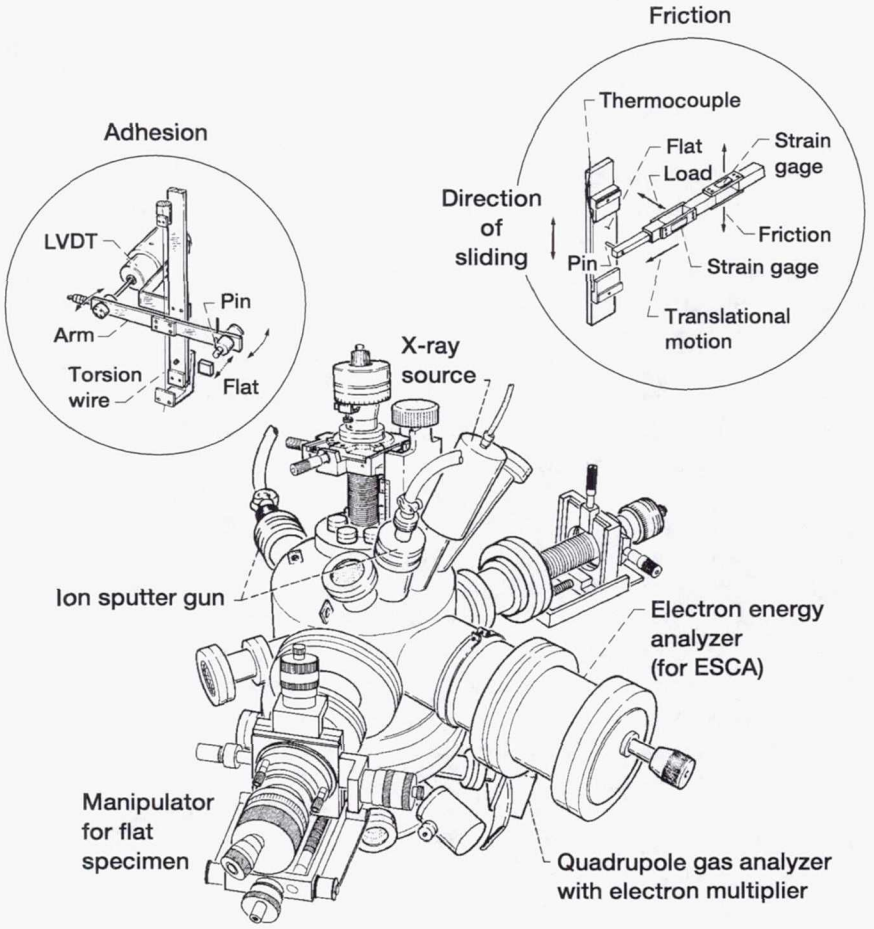

Figure 3.1.—Apparatus for measuring adhesion and friction in ultrahigh vacuum.

3.2 Adhesion Behavior

When smooth, atomically clean solid surfaces are brought into contact under a normal load, the atoms must be in contact at some points. Thus, interatomic forces will come into play [3.1, 3.2, 3.12] and cause some adhesion at these points.

Adhesion, a manifestation of mechanical strength over an appreciable area, has many causes, including chemical bonding, deformation, and the fracture processes involved in interface failure [3.1, 3.2, 3.13–3.21]. Adhesion undoubtedly depends on the area of real contact, the micromechanical properties of the interface, and the modes of junction rupture. However, there is no satisfactory theory or experimental method for determining the area of real contact. Vibration, which may cause junction (contact area) growth in the contact zone, and the environment also influence the adhesion and deformation behaviors of solids. There are many unknown and unresolved problems. Therefore, adhesion studies of solids are best performed only through refined experiments under carefully controlled laboratory conditions, such as in an ultrahigh vacuum or in an inert gas, to reduce secondary effects.

In practical cases, adhesion develops in the film formation processes of joining, bonding, and coating. Beneficially, it is a crucial factor in the structural performance of engineering materials, including monolithics, composites, and coatings, used in engines, power trains, gearboxes, and bearings [3.22–3.27]. The joining of solid to solid, fiber to matrix, and coating to substrate is determined by adhesion. Destructively, adhesion occurs during friction and wear in solid-state contacts, causing high friction and heavy surface damage.

We can use a variety of methods to quantify bonding forces. Some, such as pull-off force measurements, involve tensile pulling on the interface. Others, such as friction force measurements, are based on tangential shearing of the junction [3.3]. The stronger the interfacial bond strength, the greater the resistance to separate (pull off) or to move one surface relative to the other normally or tangentially. Such measurements are sufficiently sensitive that the adhesive bond forces for different-material couples, when two atomically clean material surfaces are brought into solid-state contact, can be readily quantified.

A torsion balance was used to measure adhesion in this study. The balance was adapted from the principle of the Cavendish balance used to measure gravitational forces in 1798–99 and also from a similar balance invented by Coulomb in 1784–85 for studying electrical attraction and repulsion [3.28, 3.29].

The adapted torsion balance [3.10, 3.11] consists of a solid (A) and a displacement sensor, such as an electromechanical transducer, mounted at opposite ends of a horizontal arm (Fig. 3.2). The arm is supported at its center by a vertical wire, perhaps a single strand of music wire. Another solid (B) is moved horizontally toward solid A, presses against it, and twists the wire through a small angle with normal force—the normal loading process—thereby moving the sensor. Solid B is then gradually moved horizontally backward until the two solids are pulled apart in a normal direction—the unloading process. If the adhesive force between the two

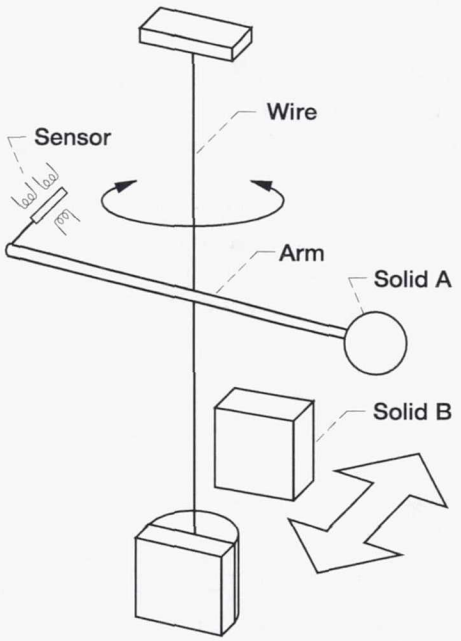

Figure 3.2.—Schematic diagram of torsion balance adapted from Cavendish balance.

solids is zero, solid A separates from solid B at its original position and untwists the wire, thereby moving the sensor back to its original position. If an adhesive force is present between the two solids, the force twists the wire as solid B moves backward until the wire develops sufficient force to separate the surfaces of solids A and B in the normal direction.

In this system the attractive force of adhesion and the force required to pull the surfaces of two solids apart (the pull-off force) act along a horizontal direction and are not affected by gravity and buoyancy. The axis of weight and buoyancy for all the components (the arm, sensor, and wire) is different from that of the pull-off microforce to be measured and is in the vertical direction because of gravity.

Because the pull-off force is measured by the torsional moment acting on the torsion wire, the force can be calibrated in three ways:

1. By calculation from the geometrical shape of the torsion wire, such as its length and area of section

2. By calculation from measured natural periods of the arm's harmonic motion when it is freely oscillating

3. By direct comparison of microforce with standard weight when the arm and torsion wire are held horizontally

The pull-off forces determined by all three methods of calibration were nearly the same [3.10].

For the actual balance shown in Fig. 3.1 the pin specimen (corresponding to solid A in Fig. 3.2) was mounted at one end of a movable arm. A free-moving, rod-shaped magnetic core was mounted on the other end of the arm. The coils of a linear variable differential transformer (LVDT) were mounted on a stationary arm. There was no physical contact between the movable magnetic core and the coil structure. The movable arm was supported by a single strand of music wire acting as a torsion spring. The flat (corresponding to solid B in Fig. 3.2) was mounted on a specimen attached to a manipulator, allowing electron beam specimen heating in a vacuum. Therefore, measurements could be made in ultrahigh vacuum, even to temperatures as high as 1200 °C.

For in situ pull-off force (adhesion) measurements in vacuum the flat specimen was brought into contact with the pin specimen by moving the micrometer headscrew forward manually. Contact was maintained for 30 s; then the pin and flat specimen surfaces were pulled apart by moving the micrometer headscrew backward. An LVDT monitored the displacement of the pin specimens. Figure 3.3 shows a typical force-time trace resulting from such adhesion experiments. Contact occurred at point A. The line A–B represents the region where load was being applied. The displacement B–X corresponds to the normal load. The line B–C represents the region where the contact was maintained at the given load and the specimen surfaces were stationary. The line C–D represents the region where both the unloading point and the separation forces were being applied on the adhesion joint. The onset of separation occurred at point D. The displacement D–Y corresponds to the pull-off force. After the pin specimen separated from the flat, the pin fluctuated back and forth, as represented by the D–E region.

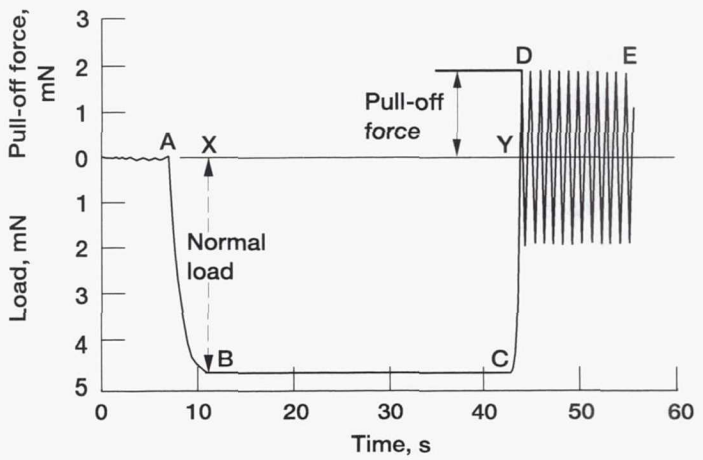

Figure 3.3—Typical force-time trace.

Atomically clean solids will exhibit strong adhesive bonds when brought into solid-state contact. A number of bulk and surface properties of solids have been shown to affect the nature and magnitude of the adhesive bond forces that develop for solids. Surface properties include electronic surface states, ionic species present at the surface, chemistry, and the surface energy of the contacting materials. Bulk properties include elasticity, plasticity, fracture toughness, cohesive bonding energy, defects, and the crystallography of the materials.

Figure 3.4 presents the pull-off force, which reflects interfacial adhesion, measured for various argon-ion-sputter-cleaned metals in contact with argon-ion-

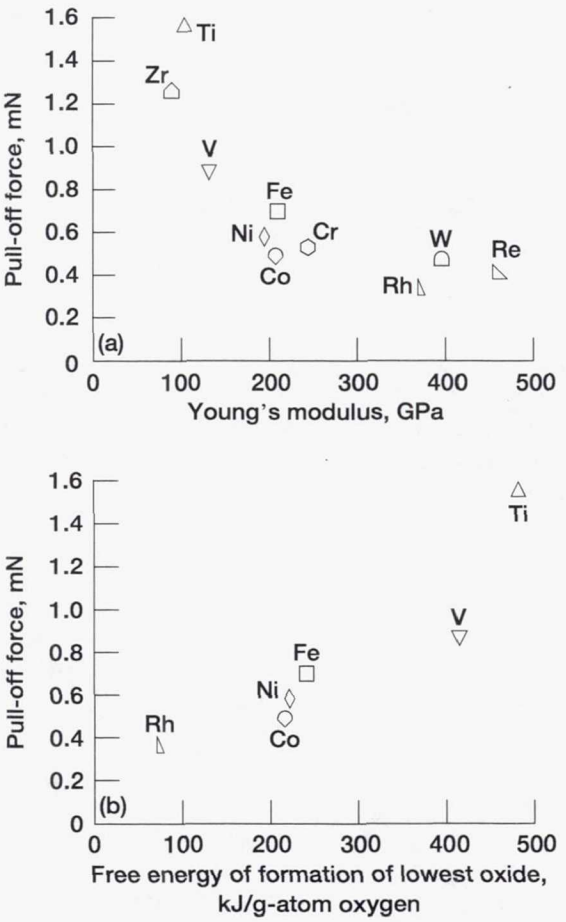

Figure 3.4.—Pull-off force (adhesion) for various metals in contact with ferrites ($MnO–ZnO–Fe_2O_3$) in ultrahigh vacuum. (a) As function of Young's modulus of metal. (b) As function of free energy of formation of lowest metal oxide.

TABLE 3.1.—CONDITIONS OF EXPERIMENTS IN ULTRA-HIGH-VACUUM ENVIRONMENT

[Hemispherical pin (0.79-mm radius) and flat specimens were polished with 3-μm diamond powder and 1-μm sapphire powder, respectively. Both specimens were argon sputter cleaned.]

Condition	Adhesion (pull-off force) measurements	Friction measurements
Load, N	0.0002 to 0.002	0.05 to 0.5
Vacuum, Pa	10^{-8}	10^{-8}
Temperature, °C	23	23
Motion	Axial	Unidirectional sliding
Sliding velocity, mm/min	----------	1
Total sliding distance, mm	----------	2.5 to 3

sputter-cleaned ferrites in ultrahigh vacuum. Table 3.1 (from [3.10]) gives the conditions of the adhesion experiments. As Fig. 3.4(a) shows, pull-off force decreased as the Young's modulus E (also known as the elastic modulus) of the metal increased. Thus, the bulk properties of the metal, such as Young's modulus, affect the magnitude of the adhesive bond forces that develop at the metal-ceramic interface. Similar pull-off force (adhesion) results were obtained for clean metal–silicon nitride (Si_3N_4) couples [3.10, 3.11].

Figure 3.4(b) shows that the pull-off forces for clean metal-ferrite couples increased as the free energy of formation of the lowest metal oxides increased. This correlation suggests that the adhesive bond at the metal-ceramic interface is a chemical bond between the metal atoms on the metal surface and the large oxygen anions on the ferrite ($MnO–ZnO–Fe_2O_3$) surface. Further, Fig. 3.4(b) indicates that the strength of this chemical bond is related to the oxygen-to-metal bond strength in the metal oxide. Similar adhesion behavior has been noted with other oxide ceramics, such as nickel-zinc ferrite ($NiO–ZnO–Fe_2O_3$) and sapphire (Al_2O_3) [3.10, 3.30].

3.3 Friction

In situ friction experiments were conducted with the friction device shown in Fig. 3.1. Table 3.1 gives the conditions of the friction experiments.

Figure 3.5 presents the coefficient of friction, which reflects interfacial adhesion, measured for various argon-ion-sputter-cleaned metals in contact with argon-ion-sputter-cleaned ferrites in ultrahigh vacuum. As Fig. 3.5(a) shows, the coefficient of friction decreased as the shear modulus of the metal G increased. Thus, the bulk properties of the metal, such as shear modulus (also known as the torsion modulus or the modulus of rigidity), play an important role in the friction behavior of clean metal-ferrite couples. The similar shapes of Figs. 3.4(a) and 3.5(a) are not surprising because $E \approx 2.6G$ (as discussed in [3.31] and briefly later).

Figure 3.5(b) shows that the coefficient of friction increased as the free energy of formation of the lowest metal oxides increased. This correlation suggests that the

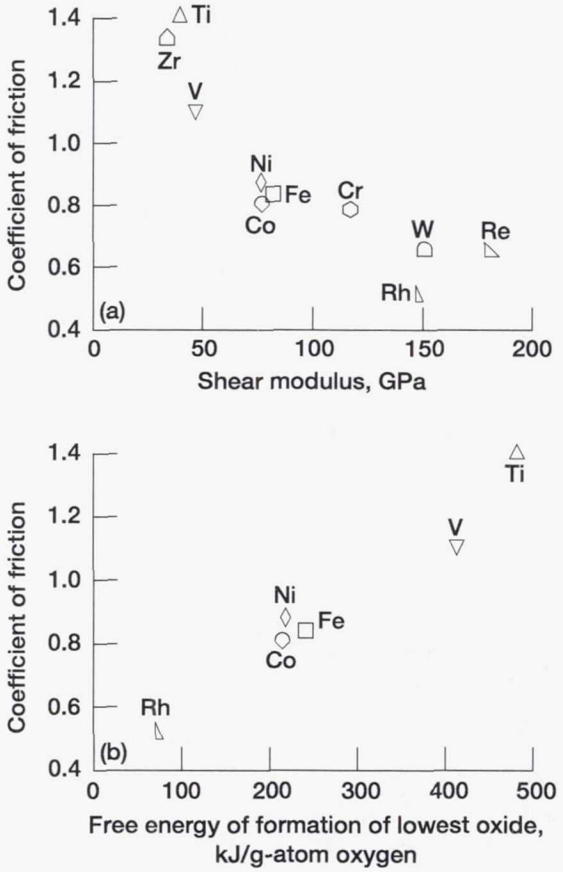

Figure 3.5.—Coefficient of friction for various metals in contact with ferrites ($MnO–ZnO–Fe_2O_3$) in ultrahigh vacuum. (a) As function of shear modulus of metal. (b) As function of free energy of formation of lowest metal oxide.

adhesive bond at the metal-ceramic interface is a chemical bond between the metal atoms on the metal surface and the large oxygen anions on the ferrite ($MnO–ZnO–Fe_2O_3$) surface (as shown in Fig. 3.6). It also suggests that the strength of this chemical bond is related to the oxygen-to-metal bond strength in the metal oxide. Similar relationships have been observed with $NiO–ZnO–Fe_2O_3$ [3.9]. This dependence of friction on the shear modulus and chemical activity of the metal is analogous to the adhesion behavior described in the previous section.

Figure 3.6(a) illustrates the spinel crystal structure of manganese-zinc (Mn-Zn) ferrite. In the unit cell, which contains 32 oxygen ions, there are 32 octahedral sites and 64 tetrahedral sites. Sixteen of the octahedral sites are filled with equal amounts

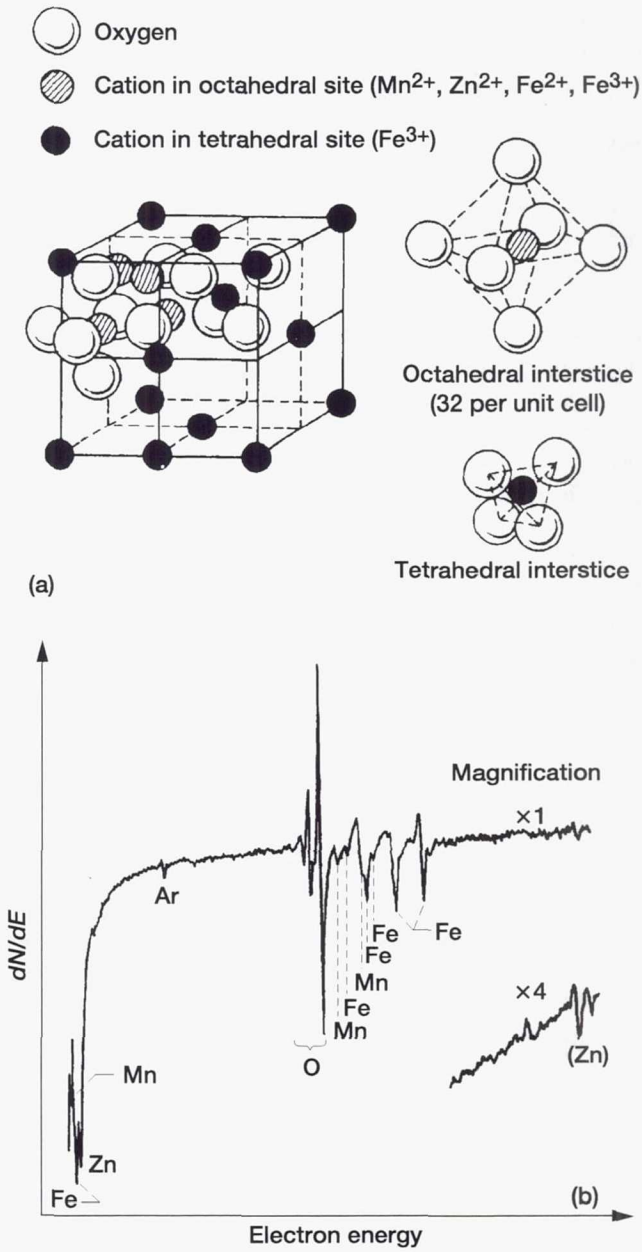

Figure 3.6.—Structure and surface of Mn-Zn ferrite. (a) Spinel structure. (b) AES spectrum for {110} surface after sputter cleaning.

of divalent (Mn^{2+}, Zn^{2+}, and Fe^{2+}) and trivalent (Fe^{3+}) ions, and eight of the tetrahedral sites are filled with trivalent (Fe^{3+}) ions [3.32, 3.33]. The Auger peaks in Fig. 3.6(b) indicate that, in addition to oxygen and iron, small amounts of manganese and zinc occur on a clean Mn-Zn ferrite surface. The surface accommodated slightly more oxygen with the {110} plane than with the {211}, {111}, and {100} planes, in that order.

The values of the Young's and shear moduli used in this investigation of bulk polycrystalline metal were those reported by Gschneidner [3.31]. Young's modulus varies from 3.538 GPa (0.0361×10^6 kg/cm^2) for potassium to 1127 GPa (11.5×10^6 kg/cm^2) for diamond. Estimated values, however, would indicate that the lower limit is probably 1.6 GPa (0.017×10^6 kg/cm^2) for francium. A recent calculation for a hypothetical material, carbon nitride in β-C_3N_4 structure, predicted a bulk modulus comparable to that for diamond (β = 410 to 440 GPa) [3.34, 3.35]. Gschneidner reported that the ratio of Young's modulus to shear modulus is essentially constant (at nearly 2.6) and that the shear modulus, like Young's modulus, markedly depends on the metal's electron configuration (i.e., the group in which it lies). The maximum value encountered in a given period of the periodic table is associated with the elements having the most unpaired d electrons. The minimum near the end of each period occurs for the elements having an s^2p^1 configuration.

The adhesion and friction behaviors described here for oxide ceramics, such as ferrites, in contact with metals are not unique to oxide ceramics. Analogous behaviors occur for metals in contact with other nonmetallic materials.

3.4 Wear

Inspection of all the metal and ceramic surfaces after sliding contact revealed that the metal deformation was principally plastic and that the cohesive bonds in the metal fractured [3.36–3.38]. All the metals that were examined failed by shearing or tearing and were transferred to the ceramic during sliding. Because the interfacial bond between the metal and the ceramic is generally stronger than the cohesive bond within the metal, separation generally took place in the metal when the junction was sheared. Pieces of the metal were torn out and transferred to the ceramic surface. For example, when an atomically clean silicon carbide (SiC) surface was brought into contact with a clean aluminum surface, the interfacial adhesive bonds that formed in the area of real contact were so strong that shearing or tearing occurred locally in the aluminum. Consequently, aluminum wear debris particles were transferred to the SiC surface during sliding, as verified by a scanning electron micrograph and an aluminum K_α x-ray map (Fig. 3.7).

The morphology of metal transfer to ceramic revealed that metals with a low shear modulus exhibited much more wear and transfer than those with a higher shear modulus. Further, the more chemically active the metal, the greater was the metal wear and transfer to the ceramic.

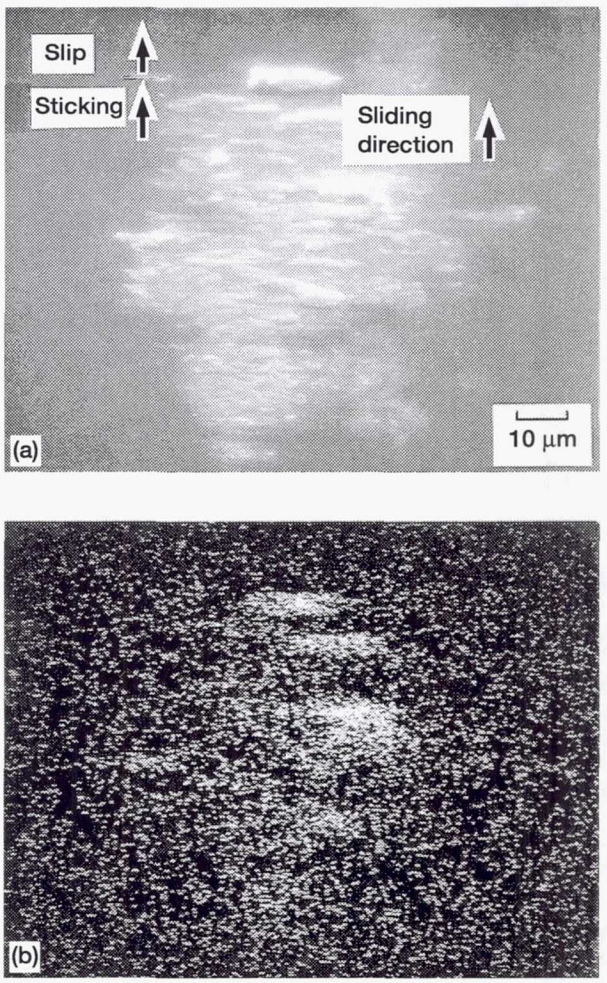

Figure 3.7.—Aluminum transferred to SiC {0001} surface before and after single-pass sliding in ultrahigh vacuum. (a) Initial contact area. (b) Aluminum K_α x-ray map (1.5×10^4 counts). (c) Aluminum wear debris.

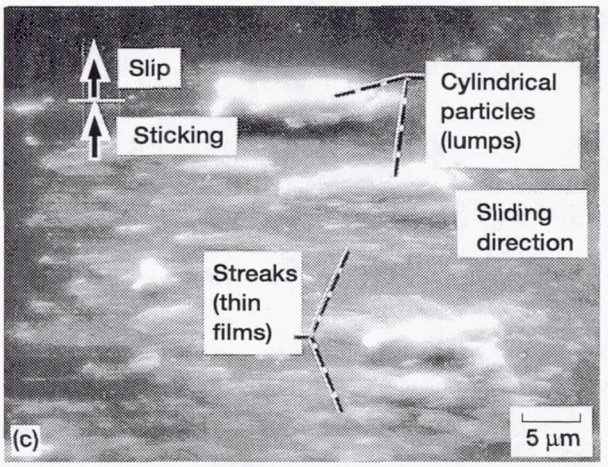

Figure 3.7.—Concluded. (c) Aluminum wear debris.

TABLE 3.2—METALS TRANSFERRED TO SiC {0001} SURFACES AFTER 10 SLIDING PASSES IN ULTRAHIGH VACUUM

Metal	Form (size) of metal transferred				Extent of metal transfer	Shear modulus, GPa
	Small particle[a]	Piled-up particles[b]	Multilayer agglomeration	Large lump particle[b]		
Al	Yes	Yes	Yes	No	Most	27
Zr	Yes	Yes	Yes	No		34
Ti	Yes	Yes	Yes	No		39
Ni	Yes	Yes	No	No		75
Co	Yes	Yes	No	No		76
Fe	Yes	Yes	No	No		81
Cr	Yes	Yes	No	No		117
Rh	Yes	No	No	Yes		147
W	Yes	No	No	Yes		150
Re	Yes	No	No	Yes	Least	180

[a]Submicrometer.
[b]Several micrometers.

Table 3.2 summarizes the type of metal transfer to single-crystal SiC that was observed after multipass sliding. Generally, the metals at the bottom of the table had a higher shear modulus and less chemical affinity for silicon and carbon. Therefore, those metals exhibited less wear and transferred less metal to the SiC.

Note that sometimes the strong adhesion and high friction between a metal and a ceramic can locally damage the ceramic surface if that surface contains imperfections, such as microcracks or voids [3.36–3.38].

3.5 Relationship of Material Properties to Adhesion, Friction, and Wear

The tribological properties of clean, smooth, solid surfaces depend on the physical, mechanical, and metallurgical properties of the surface. As discussed in Sections 3.2 to 3.4, the physical properties, such as the Young's and shear moduli, influence observed adhesion, friction, and wear behaviors.

3.5.1 Mechanical Properties

Theoretical tensile strength.—A clean metal in sliding contact with a clean nonmetal or with itself will fail either in tension or in shear because some of the interfacial bonds are generally stronger than the cohesive bonds in the cohesively weaker metal. The failed metal subsequently transfers to nonmetallic material or to the other contacting metal (Fig. 3.7 [3.36–3.40]). Therefore, friction, metal wear, and metal transfer should be related to the metal's chemical, physical, and metallurgical properties and strength.

As greater and greater mechanical strengths are obtained from engineering materials, it is only logical to ask what the upper limit may be to the strength of a solid. This upper limit, or maximum strength, has come to be referred to as "the theoretical tensile strength." Therefore, let us consider first the relationship between theoretical tensile strength and tribological properties [3.41].

The generally accepted thinking on solid fracture is that the ideal elastic solid exhibits elastic response to a load until the interatomic forces are overcome and atomic separation takes place on a plane. At the atomistic level, fracture occurs when the bonds between atoms are broken across a fracture plane, creating a new surface. Bonds can be broken perpendicular to the fracture plane (Fig. 3.8(a)) or sheared across the fracture plane (Fig. 3.8(b)). Such behavior is expected for an ideal crystalline solid with no defects. Under such conditions the criteria for fracture are simple: fracture occurs when the local stress builds up either to the theoretical cohesive strength or to the theoretical shear strength.

The theoretical cohesive strength of an ideal elastic solid is calculated on the basis of all the energy used in separation being available for creating the two new surfaces. The surface energy is assumed to be the only energy expended in creating these surfaces. If the atoms A and A′ in Fig. 3.8(a) are pulled apart, the stress required to separate the plane is the theoretical uniaxial tensile strength σ_{max}. When that strength is reached, the bonds are broken. That strength is given by the well-known equation

$$\sigma_{max} = \sqrt{\frac{E\gamma}{d}} \tag{3.1}$$

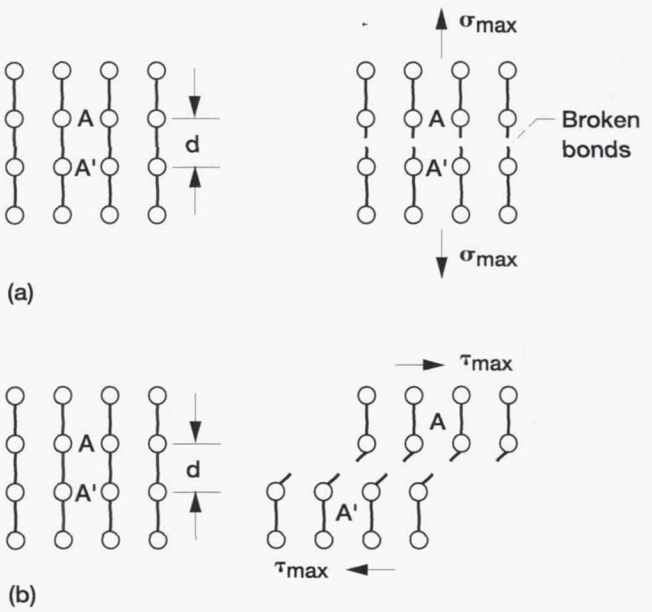

Figure 3.8.—Fracture viewed at atomistic level in terms of breaking of atomic bonds. (a) Tensile fracture. (b) Shear fracture.

where E is the appropriate Young's modulus, γ is the surface energy per unit area, and d is the interplanar spacing of the planes perpendicular to the tensile axis [3.42–3.46]. In this equation the theoretical tensile strength of the solid is directly related to other macroscopic physical properties.

The foregoing approach is equally applicable to any solid. Frenkel used a similar method to estimate the theoretical shear strength τ_{max} of a solid subjected to a simple shear mode of deformation [3.42, 3.47]. He assumed that, for any solid, the stress required to shear any plane a distance x over its neighbor is given by

$$\tau = \kappa \sin \frac{2\pi x}{b} \tag{3.2}$$

where b is the appropriate repeat distance in the shear direction (the planes are assumed to be undistorted by the shear) and κ is chosen to give the correct shear modulus G. It is then easily shown that

$$\tau_{max} = \frac{Gb}{2\pi d} \tag{3.3}$$

where d is the interplanar spacing of the shearing planes.

Figure 3.9 presents the coefficient of friction as a function of the theoretical tensile strength σ_{max}. (The values of σ_{max} can be obtained from Eq. (3.1).) There generally appears to be a strong correlation between friction and σ_{max}, with the friction decreasing as the theoretical tensile strength of the metals increased. The higher the tensile strength, the lower the friction.

When metallic and nonmetallic materials in sliding contact separate, fracture occurs in the metal as well as shear at the adhesive bonds in the interface. The morphology of metal transfer to nonmetal revealed that metals with low tensile strength exhibited much more transfer than those with higher tensile strength. For example, examination of wear tracks on SiC after single-pass sliding with titanium revealed evidence that both thin films and lump particles of titanium had transferred to the SiC. On the other hand, examination of the SiC surface after multipass sliding with titanium indicated the presence of thin transfer films, multilayer transfer films, small particles, and pileup of particles. Table 3.2 summarizes the metal transfer to single-crystal SiC observed after multipass sliding. Generally, metals closer to the bottom of Table 3.2 have less chemical affinity for silicon and carbon and greater resistance to tensile and shear fracture and, accordingly, lower coefficients of friction. Therefore, less transfer to SiC was observed with these metals.

Such dependency of metal transfer on the theoretical tensile strength arises from the adhesion and fracture properties of the metal. Thus, theoretical tensile strength, which is a function of surface energy, Young's modulus, and interplanar spacing in the crystal, plays a role in the adhesion, friction, and transfer of metals contacting metals or nonmetals. Surface energies of solid metals have been reported in the literature [3.48–3.56]. Investigators have sought correlations between surface energy and other physical properties [3.48, 3.49, 3.56]. The most successful and widely accepted of these correlations for elemental solids occurs where the heat of sublimation has been considered. A good correlation between surface and cohesive energy was also, however, found by Tyson and Jones [3.48, 3.49]. The correlation between surface energy and tribological properties will be sought later, in Section 3.6.

Theoretical shear strength.—Theoretical shear strength values were obtained from Eq. (3.3) and are presented in Table 3.3. It was assumed that the slip plane is in the slip direction, as indicated in Table 3.3.

Figure 3.10 presents the coefficient of friction as a function of the theoretical shear strength τ_{max}. These data show that the friction decreased as the theoretical shear strength of the metal bond increased. The theoretical shear strength generally correlated with the coefficient of friction for metals in contact with such nonmetals as diamond, pyrolytic boron nitride (BN), SiC, and Mn-Zn ferrite, as shown in Figs. 3.10(a) to (d). The coefficients of friction for metals in contact with themselves correlated with the metal's shear strength, except for platinum and palladium, as indicated in Fig. 3.10(e). In creating these figures the shear strength values for face-centered cubic metals from Table 3.3 were used. The shear strength values for the body-centered cubic metals were average values calculated from the shear strengths for three dominant slip systems. Those for the hexagonal metals

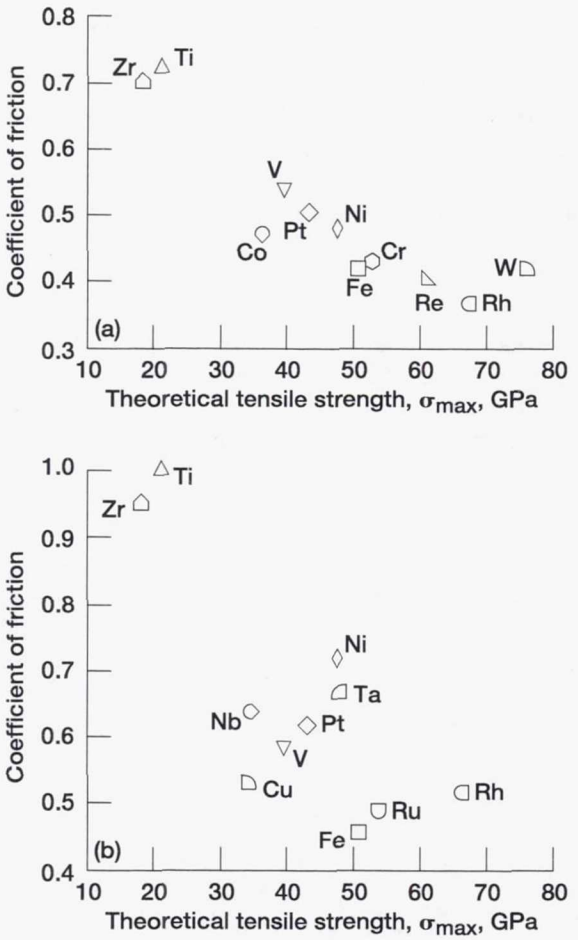

Figure 3.9.—Coefficient of friction as function of theoretical tensile strength for metals in sliding contact with nonmetals and themselves. Tensile direction: ⟨111⟩ for face-centered cubic, ⟨110⟩ for body-centered cubic, and ⟨0001⟩ for hexagonal metals; room temperature; vacuum pressure, 10^{-8} Pa. (a) Sliding material, single-crystal diamond {111} surface; sliding direction, $\langle 1\bar{1}0 \rangle$; sliding velocity, 3 mm/min; load, 0.05 to 0.3 N. (b) Sliding material, pyrolitic BN surface; sliding velocity, 0.77 mm/min; load, 0.3 N. (c) Sliding material, single-crystal SiC {0001} surface; sliding direction, $\langle 10\bar{1}0 \rangle$; sliding velocity, 3 mm/min; load, 0.05 to 0.5 N. (d) Sliding material, single-crystal Mn-Zn ferrite {110} surface; sliding direction, $\langle 1\bar{1}0 \rangle$; sliding velocity, 3 mm/min; load, 0.3 N. (e) Sliding materials, metals against themselves; sliding velocity, 0.7 mm/min; load, 0.01 N.

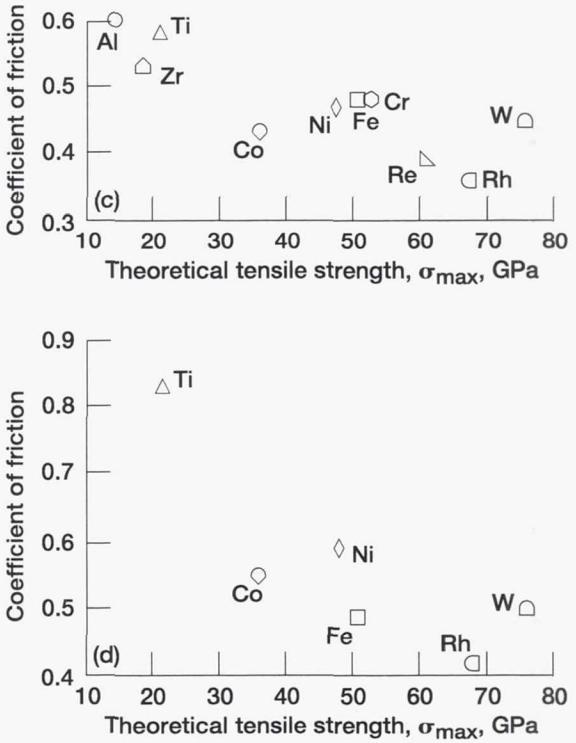

Figure 3.9.—Continued. (c) Sliding material, single-crystal SiC {0001} surface; sliding direction, $\langle 10\bar{1}0 \rangle$; sliding velocity, 3 mm/min; load, 0.05 to 0.5 N. (d) Sliding material, single-crystal Mn-Zn ferrite {110} surface; sliding direction, $\langle 1\bar{1}0 \rangle$; sliding velocity, 3 mm/min; load, 0.3 N.

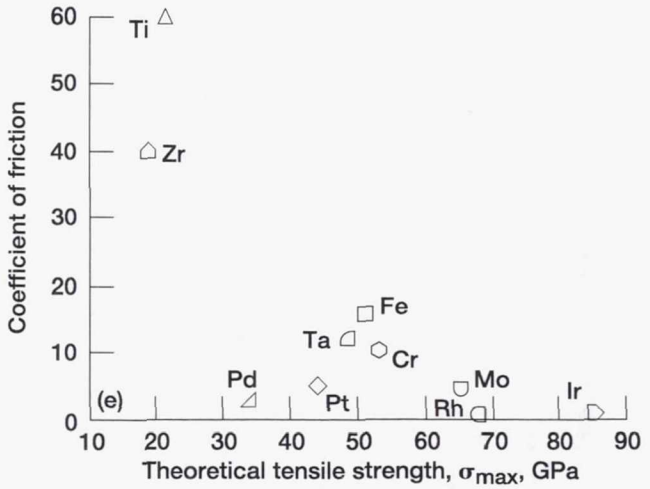

Figure 3.9.—Concluded. (e) Sliding materials, metals against themselves; sliding velocity, 0.7 mm/min; load, 0.01 N.

were average values calculated from the shear strengths for two dominant slip systems (i.e., the $\langle 10\bar{1}0 \rangle \langle 10\bar{1}0 \rangle$ and $\{0001\} \langle 11\bar{2}0 \rangle$).

Thus, tensile and shear properties were shown to play important roles in the adhesion and friction of metals contacting nonmetals or metals contacting themselves. However, these simple calculations of the theoretical strength and the correlation between friction and strength can be criticized on several grounds. The extent of slip in a crystal varies with the magnitude of the shear stresses produced by the applied forces and the crystal's orientation with respect to these applied forces. This variation can be rationalized by the concept of the crystal's resolved shear stress for slip. Despite the foregoing, the relationship between the coefficient of friction and the theoretical shear strength may lead to an appreciation of how the physical properties of materials determine their tribological properties and mechanical behavior.

A good correlation between the coefficient of friction and the shear modulus (e.g., Fig. 3.5(a)) was also found for metals contacting nonmetals. The correlation is similar to that between the coefficient of friction and the shear strength (refer to Fig. 3.10). This similarity is to be expected because, as shown in Table 3.3, the ratio τ_{max}/G is essentially constant.

Actual shear strength.—The theoretical shear and tensile strengths are much greater than commonly found experimentally. In the previous sections the relationships between these theoretical strengths and the friction properties of metals in contact with nonmetals and with themselves were discussed. There is, in addition, an obvious need to compare the actual observed strengths of metals with their friction properties.

TABLE 3.3—SIMPLE CALCULATIONS OF THEORETICAL SHEAR STRENGTH

(a) Face-centered cubic structure; shear plane and direction, $\{111\}, \langle 110 \rangle$

Metal	Shear strength, τ_{max}, GPa	Strength to modulus ratio, τ_{max}/G
Al	2.6	0.096–0.098
Ni	7.3	↓
Cu	4.4	↓
Rh	15	↓
Pd	5.0	↓
Ir	21	↓
Pt	5.9	↓

(b) Body-centered cubic structure

Metal	Shear plane and direction					
	$\{110\}\langle 111\rangle$		$\{112\}\langle 111\rangle$		$\{123\}\langle 111\rangle$	
	τ_{max}, GPa	τ_{max}/G	τ_{max}, GPa	τ_{max}/G	τ_{max}, GPa	τ_{max}/G
V	3.1	0.65–0.66	5.3	0.11	8.1	0.17
Cr	7.6	↓	13	↓	20	↓
Fe	5.3	↓	9.2	↓	14	↓
Nb	2.4	↓	4.2	↓	6.4	↓
Mo	7.5	↓	13	↓	20	↓
Ta	4.5	↓	7.8	↓	12	↓
W	9.8	↓	17	↓	26	↓

(c) Close-packed hexagonal structure

Metal	Shear plane and direction					
	$\{0001\}\langle 11\bar{2}0\rangle$		$\{10\bar{1}0\}\langle 11\bar{2}0\rangle$		$\{10\bar{1}1\}\langle 11\bar{2}0\rangle$	
	τ_{max}, GPa	τ_{max}/G	τ_{max}, GPa	τ_{max}/G	τ_{max}, GPa	τ_{max}/G
Ti	3.9	0.098–0.10	7.2	0.18–0.19	8.2	0.21
Co	7.5	↓	14	↓	16	↓
Y	2.6	↓	4.8	↓	5.5	↓
Zr	3.4	↓	6.3	↓	7.1	↓
Ru	16	↓	29	↓	34	↓
Re	18	↓	33	↓	38	↓

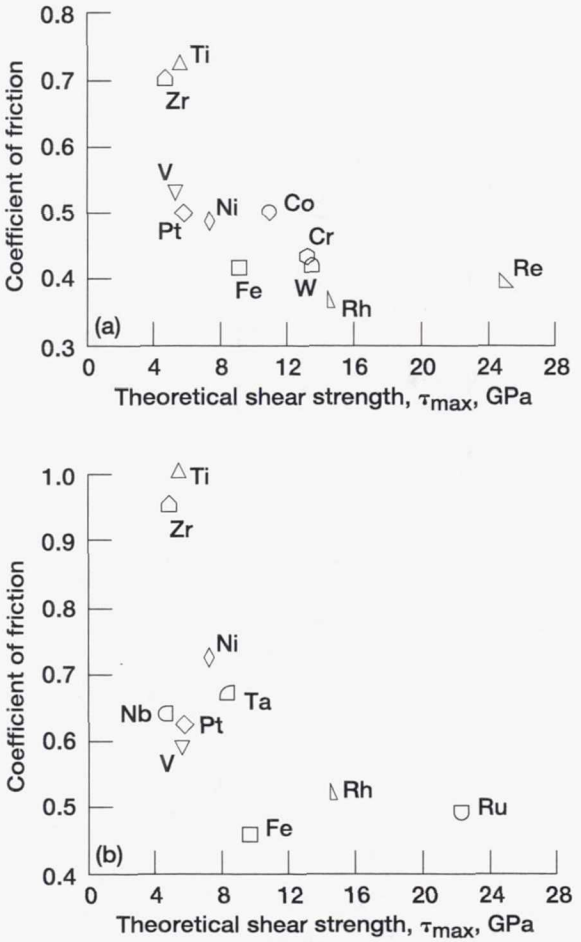

Figure 3.10.—Coefficient of friction as function of theoretical shear strength for metals in sliding contact with nonmetals and themselves. Room temperature; vacuum pressure, 10^{-8} Pa. (a) Sliding material, single-crystal diamond {111} surface; sliding direction, $\langle 1\bar{1}0 \rangle$; sliding velocity, 3 mm/min; load, 0.05 to 0.3 N. (b) Sliding material, pyrolytic BN surface; sliding velocity, 0.77 mm/min; load, 0.3 N. (c) Sliding material, single-crystal SiC {0001} surface; sliding direction, $\langle 10\bar{1}0 \rangle$; sliding velocity, 3 mm/min; load, 0.05 to 0.5 N. (d) Sliding material, single-crystal Mn-Zn ferrite {110} surface; sliding direction, $\langle 1\bar{1}0 \rangle$; sliding velocity, 3 mm/min; load, 0.3 N. (e) Sliding materials, metals against themselves; sliding velocity, 0.7 mm/min; load, 0.01 N.

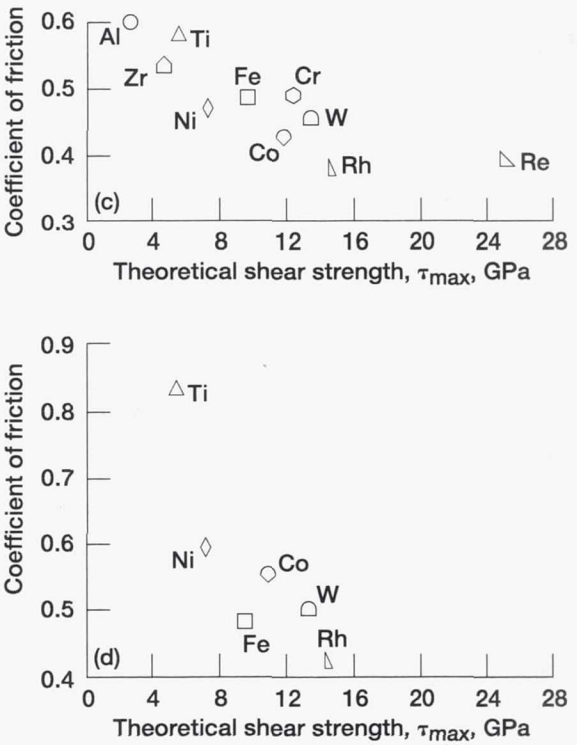

Figure 3.10.—Continued. (c) Sliding material, single-crystal SiC {0001} surface; sliding direction, ⟨1010⟩;
sliding velocity, 3 mm/min; load, 0.05 to 0.5 N.
(d) Sliding material, single-crystal Mn-Zn ferrite {110} surface; sliding direction, ⟨110⟩; sliding

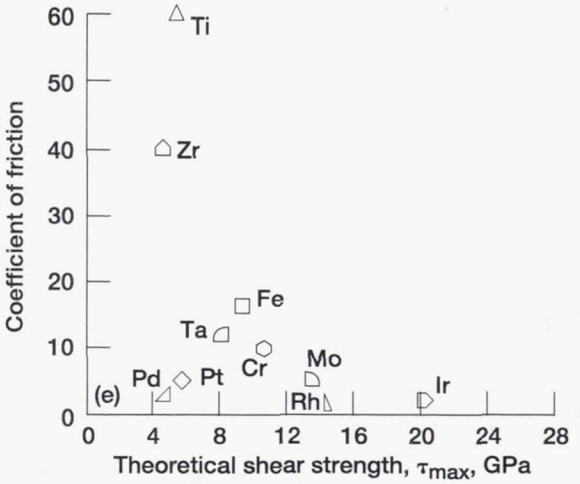

Figure 3.10.—Concluded. (e) Sliding materials, metals against themselves; sliding velocity, 0.7 mm/min; load, 0.01 N.

The actual shear strengths of metals were estimated from Bridgman's experimental data [3.57]. The shear phenomena and strengths were studied at high hydrostatic pressures (to 4.9 GPa). The shear strength of a metal strongly depended on the hydrostatic pressure acting on it during shear, increasing as applied hydrostatic pressure increased. The actual shear strengths were estimated by extrapolating from the contact pressure during sliding experiments by using Bridgman's relationships between hydrostatic pressure and shear strength. The contact pressures for various metals in contact with nonmetals were calculated by using Hertz's classical equations [3.58].

Figure 3.11 presents the coefficient of friction for metals in contact with clean diamond, SiC, and Mn-Zn ferrite as a function of the actual shear strength. Generally, friction decreased as the actual shear strength increased. This correlation seems to indicate that the ratio of actual to theoretical shear strength does not vary greatly from one elemental metal to another.

Thus, the coefficients of friction for clean metals in contact with clean diamond, BN, SiC, Mn-Zn ferrite, and metals in ultrahigh vacuum can be generally related to the theoretical tensile, theoretical shear, and actual shear strengths of the metals. The stronger the metal, the lower the coefficient of friction.

Hardness.—In general, hardness implies resistance to deformation [3.59, 3.60]. With elastic materials, such as rubber, the elastic properties play an important role in assessing hardness. With inorganic materials, such as metals and ceramics, however, the position is different, for although their elastic moduli are generally large, metals and ceramics deform elastically over a relatively small range, predominantly outside the elastic range. Consequently, considerable plastic or

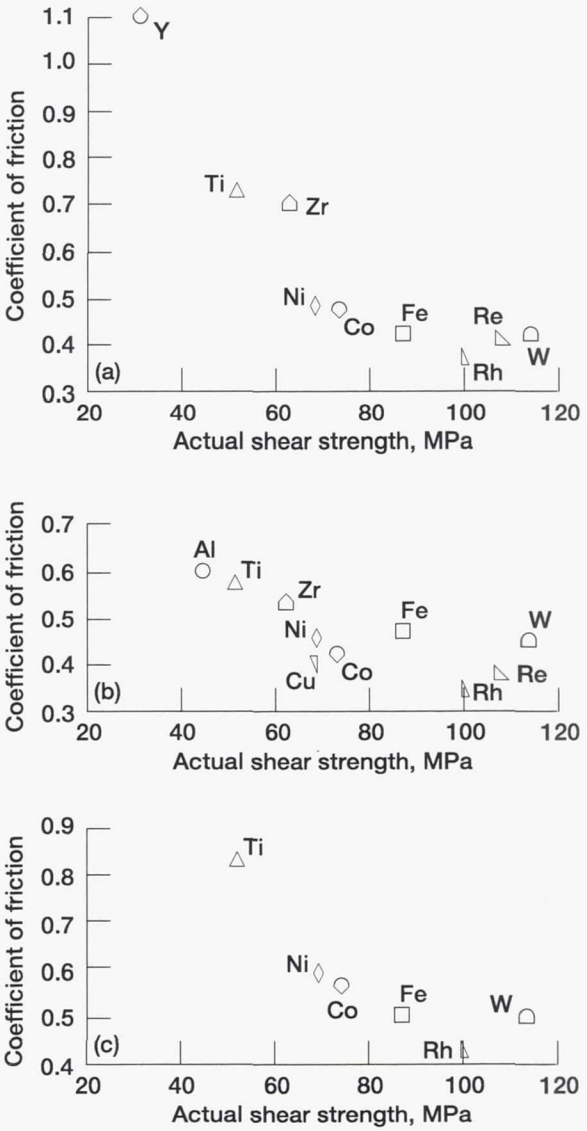

Figure 3.11.—Coefficient of friction as function of actual metal shear strength for single-crystal metals in sliding contact with various polycrystalline materials. Sliding direction, $\langle 1\bar{1}0 \rangle$; sliding velocity, 3 mm/min; room temperature; vacuum pressure, 10^{-8} Pa. *(a) Diamond {111} surface. (b) SiC {0001} surface.* (c) Mn-Zn ferrite {110} surface.

permanent deformation often occurs. For this reason the hardness of metals and ceramics is bound up primarily with their plastic strength properties and only to a secondary extent with their elastic properties. In ceramics the fracture properties may be as important as the plastic properties, particularly at high loads. Thus, hardness is another way of determining the plastic yield strength of a material, namely the amount of plastic deformation, produced mainly in compression, by a known force.

Hardness, like other mechanical properties, such as tensile and shear strength, is closely related to the Young's and shear moduli, as shown in Fig. 3.12. All the plotted Vickers hardness data were measured on polished metal surfaces by using a diamond pyramid indenter at a load of 0.25 N. Because the Vickers hardness of the metals increased as the shear modulus increased, their adhesion and friction are expected to be related to their hardness. Figure 3.13 shows the relationship between coefficient of friction and hardness for several metal-SiC couples. Friction decreased as hardness increased.

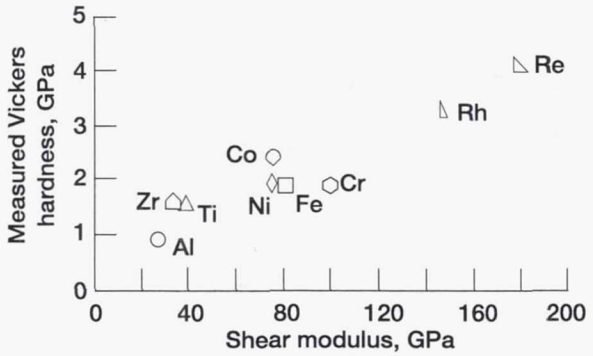

Figure 3.12.—Vickers hardness as function of shear modulus for various metals. Load, 0.25 N.

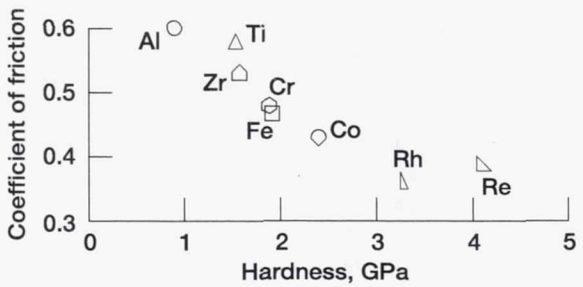

Figure 3.13.—Coefficient of friction as function of hardness for various metal-SiC couples.

3.5.2 Chemical Properties

Today, almost all the known elements are used to make ceramic materials and products. Probably the most widely used class of ceramic materials, however, is the oxides, such as sapphire (Al_2O_3) an d zirconia (ZrO_2).

All but a handful of metals, alloys, and nonoxide ceramics (e.g., SiC, Si_3N_4, and molybdenum disulfide (MoS_2)) will form surface oxide films in air by their surface chemical reactivities. The thickness of the reaction oxide products varies depending on the material's reactivity to the environment, crystallographic orientation, grain boundary, impurities, dislocations, defects, surface topography, and mechanical stresses. However, 100 nm might be considered a typical thickness for such oxide layers [3.61, 3.62].

The surface reactivity required to form oxides is related to the mechanical properties of the parent material (Fig. 3.14). The free energy of formation of the lowest metal oxide correlates with the shear modulus of the metal. The higher the shear modulus, the lower the free energy of formation.

A close relationship exists between the coefficient of friction of a clean metal-ferrite contact and the free energy of formation of the lowest metal oxide (the strength of the chemical bond). The higher the free energy of formation, the greater the adhesion and friction (Figs. 3.4 and 3.5).

In 1948, Linus Pauling formulated a resonating valence bond theory of metals and intermetallic compounds in which numerical values could be placed on the bonding character of the various transition elements [3.63]. Because the d valence bonds are not completely filled in transition metals, they are responsible for such physical and chemical properties as cohesive energy, shear modulus, chemical stability, and magnetic properties. The greater the amount or percentage of d bond character that a metal possesses, the less active is its surface. Although there have been critics of this theory, it appears to be the most plausible explanation for the interfacial interactions of transition metals in contact with ceramics as well as with themselves [3.1].

When a transition metal is placed in contact with a ceramic material in an atomically clean state, the interfacial bonds formed between the metal and the ceramic depend heavily on the character of the bonding in the metal. Figure 3.15 shows, for example, the coefficients of friction for some transition metals in contact with a single-crystal diamond {111} surface as a function of both the shear modulus and d valence bond character of the metals [3.37]. The data for these sputter-cleaned surfaces indicate that adhesion and friction decreased as d valence bond character increased, as Pauling's theory predicts. Titanium and zirconium, which are chemically very active, exhibited strong adhesive bonding to the ceramic. In contrast, rhodium and rhenium, which have a high percentage of d bond character, had relatively low adhesion and friction. Thus, the more chemically active the metal, the higher the coefficient of friction.

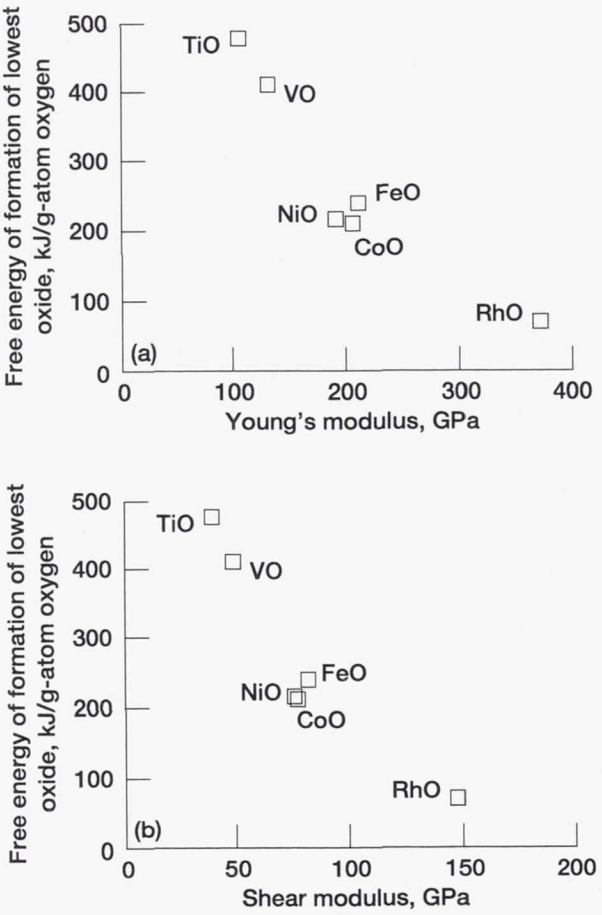

Figure 3.14.—Free energy of formation of lowest oxide. (a) As function of Young's modulus of metals. (b) As function of shear modulus of metals.

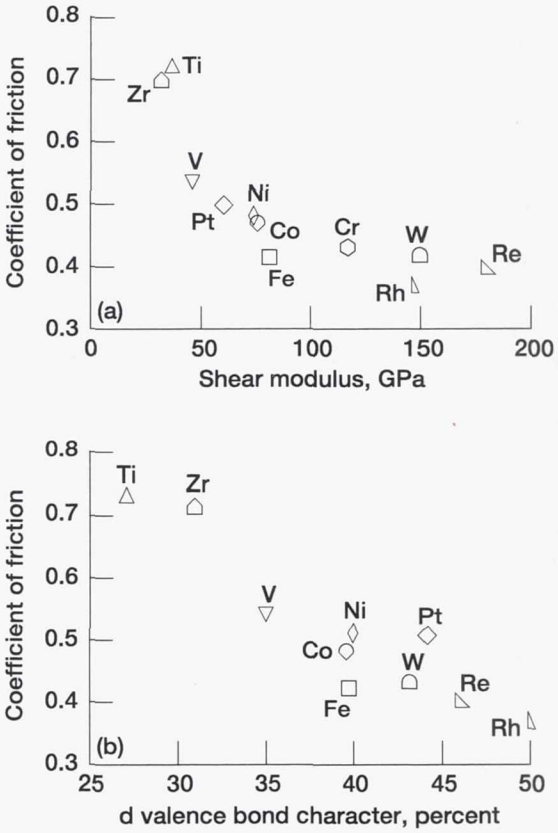

Figure 3.15.—Coefficient of friction for various metals in sliding contact with diamond {111} surface in ultrahigh vacuum. (a) As function of metal's shear modulus. (b) As function of percent of metal's d valence bond character.

3.5.3 Metallurgical Properties

There is little doubt that a solid's structure plays an important role in its mechanical behavior [3.64], particularly tribological behavior. Structure depends first on chemical composition and then on mechanical and thermal processing (sintering, casting, hot working, machining, and heat treatments of all kinds). For example, solid solution alloying is a major mode of metal strengthening. Such chemical composition and processing steps influence tribological properties by their effect on phase, concentration of ingredients and their gradients, inclusions, voids, metastable phases, dispersed phases, and lattice imperfections of different kinds [3.64].

Alloying element effects.—Figure 3.16 (from [3.65]) shows the coefficients of friction for six iron-base binary alloys in contact with single-crystal SiC as a function of solute concentration (given in Table 3.4). The coefficient of friction initially increased markedly with the presence of any alloying element and then continued to increase more gradually as the concentration of alloying element increased. The rate of increase in the coefficient of friction strongly depended on the alloying element.

The average coefficient of friction for pure iron in sliding contact with single-crystal SiC is approximately 0.5 [3.38]. This value was obtained under identical experimental conditions to those of this investigation. The coefficients of friction were about 0.6 for pure titanium, 0.5 for pure nickel and tungsten, and 0.4 for pure rhodium. The coefficients of friction for the alloys were generally much higher, as much as twice those for pure metals.

Figure 3.17 presents the average coefficients of static friction for the various alloys of Fig. 3.16 as a function of solute-to-iron atomic radius ratio. The maximum solute concentration extended to approximately 16 at.%. The good agreement between the coefficient of static friction and the solute-to-iron atomic radius ratio differed for two cases: first, alloying with manganese and nickel, which have smaller atomic radii than iron; and second, alloying with chromium, rhodium, tungsten, and titanium, which have larger atomic radii than iron. The coefficients of static friction increased generally as the solute-to-iron atomic radius ratio increased or decreased from unity. The rate of increase was much greater for the first case than for the second case. Atomic size ratios reported herein are from [3.66] and [3.67]. The correlations indicate that the atomic size of the solute is an important factor in controlling the friction in iron-base binary alloys as well as the abrasive wear and friction reported by Miyoshi and Buckley [3.66] and the alloy hardening reported by Stephens and Witzke [3.67]. The mechanism controlling alloy friction may be raising the Peierles stress and/or increasing the lattice friction stress, by solute atoms, thus resisting the shear fracture of cohesive bonds in the alloy.

More detailed examination of Fig. 3.17 indicates that the correlation for manganese, nickel, and chromium was better than that for titanium, tungsten, and rhodium. The coefficient of friction for rhodium was relatively low, and that for titanium was relatively high. The relative chemical activity of the transition metals (metals with partially filled d shell) as a group can be ascertained from their percentage of d valence bond character after Pauling [3.63]. It has already been determined [3.38] that the coefficient of friction for SiC in contact with various transition metals is related to the d valence bond character (i.e., the chemical activity) of the metal. The more active the metal, the higher the coefficient of friction. Table 3.5 shows the reciprocal d valence bond character of metals calculated from the data of Buckley [3.62]. The greater the reciprocal d valence bond character, the more active the metal and the higher the coefficient of friction [3.38].

Rhodium-iron alloys in contact with SiC showed relatively low friction, but titanium-iron alloys showed relatively high friction. The results seem to be related

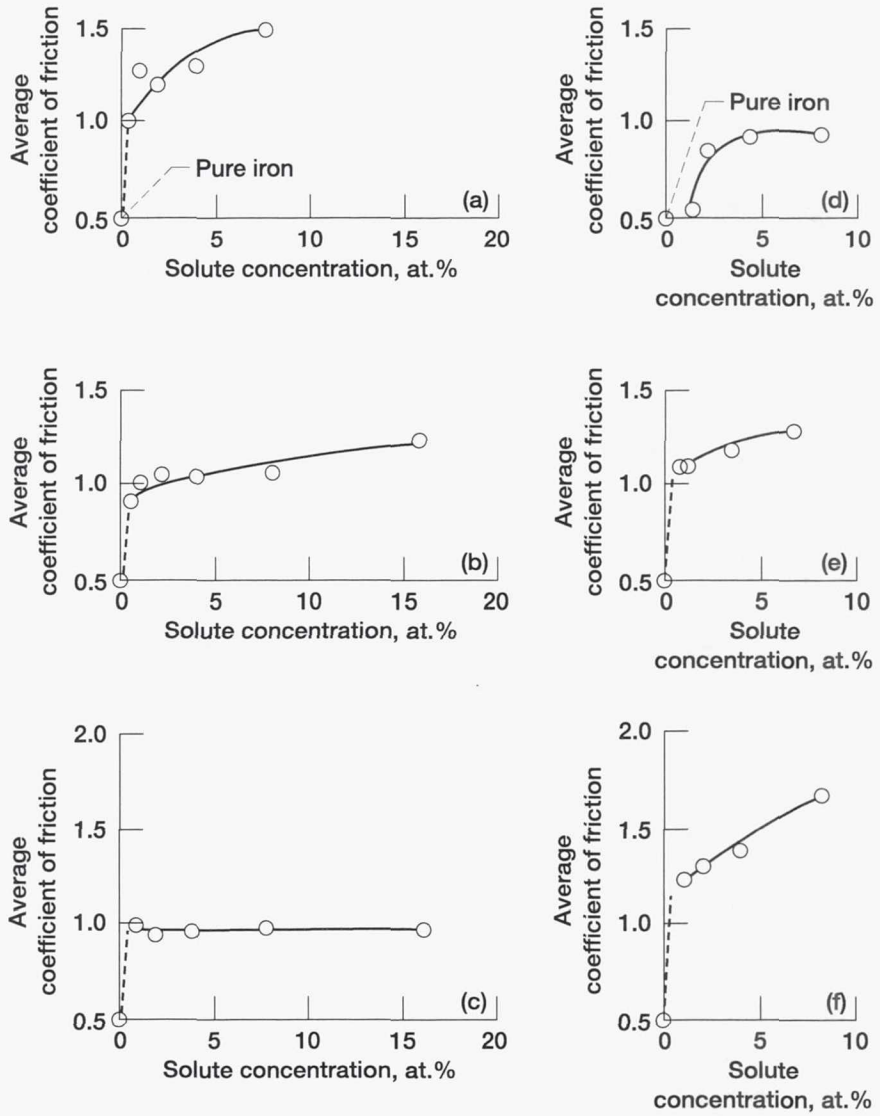

Figure 3.16.—Coefficient of friction as function of solute concentration for various iron-base binary alloys after single-pass sliding on single-crystal SiC {0001} surface. Sliding direction, $\langle 10\bar{1}0 \rangle$; sliding velocity, 3 mm/min; load, 0.2 N; room temperature; vacuum pressure, 10^{-8} Pa.

TABLE 3.4.—CHEMICAL ANALYSIS AND SOLUTE-TO-IRON ATOMIC RADIUS RATIOS FOR IRON-BASE BINARY ALLOYS

Solute element	Analyzed solute content, at.%	Analyzed interstitial content, ppm by weight			Solute-to-iron atomic radius ratio
		C	O	P	
Ti	1.02	56	92	7	1.1476
	2.08	—	—	—	
	3.86	87	94	9	
	8.12	—	—	—	
Cr	0.99	—	—	—	1.0063
	1.98	50	30	12	
	3.92	—	—	—	
	7.77	40	85	10	
	16.2	—	—	—	
Mn	0.49	—	—	—	0.9434
	.96	39	65	6	
	1.96	—	—	—	
	3.93	32	134	8	
	7.59	—	—	—	
Ni	0.51	—	—	—	0.9780
	1.03	28	90	6	
	2.10	—	—	—	
	4.02	48	24	5	
	8.02	—	—	—	
	15.7	38	49	7	
Rh	1.31	—	—	—	1.0557
	2.01	20	175	22	
	4.18	—	—	—	
	8.06	12	133	19	
W	0.83	30	140	12	1.1052
	1.32	—	—	—	
	3.46	23	61	21	
	6.66	—	—	—	

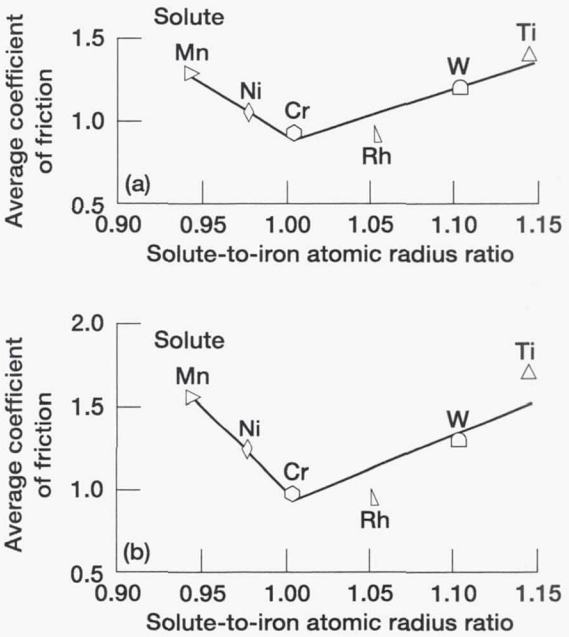

Figure 3.17.—Coefficient of friction as function of solute-to-iron atomic radius ratio for various iron-base binary alloys after single-pass sliding on single-crystal SiC {0001} surface. Sliding direction, $\langle 10\bar{1}0 \rangle$; sliding velocity, 3 mm/min; load, 0.2 N; room temperature; vacuum pressure, 10^{-8} Pa.

TABLE 3.5.—AMOUNT AND RECIPROCAL OF d VALENCE BOND CHARACTER FOR TRANSITION ELEMENTS

Metal	Amount of d character, percent	Reciprocal of d character
Fe	39.7	0.68
Mn	40.1	0.67
Ni	40.0	0.68
Cr	39	0.69
Rh	50	0.54
W	43	0.63
Ti	27	1

to the chemical activity of the alloying elements (i.e., rhodium is less active than iron and titanium is more active), as indicated in Table 3.5. The good correlation for manganese, nickel, and chromium in Fig. 3.17 is due to their reciprocal d valence bond characters being almost the same as that for iron.

Figure 3.18 presents a scanning electron micrograph and an x-ray energy dispersive map of a wear track on SiC generated by the 8.12-at.%-titanium–iron alloy pin. In the x-ray map (Fig. 3.18(b)) the concentration of white spots corresponds to those locations in the micrograph (Fig. 3.18(a)) where copious amounts of alloy have transferred. Obviously, a large amount of alloy transferred to the SiC surface. The light area in Fig. 3.18(a), where alloy transfer is evident, was the contact area before sliding of the pin. In this area the surfaces of the titanium alloy and the SiC stuck together and strong interfacial adhesion occurred. Here, both the loading and tangential (shear) forces were applied to the specimen. All single-crystal SiC surfaces after sliding contact with the alloys whose analysis is shown in Table 3.4 contained metallic elements, indicating alloy transfer to the SiC. Alloys having high solute concentrations produced more transfer than did alloys having low solute concentrations.

Figure 3.19 shows a typical pin wear scar on an iron-base binary alloy (in this case, 8.12-at.%-Ti–Fe alloy). The size of the wear scar (Fig. 3.19(a)) is comparable to the alloy transfer area shown in Fig. 3.18(a). The wear scar reveals a large number of small grooves and microcracks formed primarily by interface shearing and shearing in the alloy bulk. Close examination of Fig. 3.19(b) indicates that the cracks were small, were in the wear scar, and propagated nearly perpendicular to the sliding direction.

In summary, the atomic size misfit and the concentration of the alloying element are important factors in controlling the adhesion and friction of iron-base binary alloys in contact with SiC. The mechanism controlling alloy adhesion and friction may be raising the Peierles stress and/or increasing the lattice friction stress by solute atoms, thus resisting the shear fracture of cohesive bonds in the alloy. The coefficient of friction generally increased markedly with the presence of any concentration of alloying element in the pure metal and then increased more gradually as the concentration of alloying element increased. The coefficient of friction generally increased as the solute-to-iron atomic radius ratio increased or decreased from unity. The atomic size misfit and the concentration of alloying element were factors in controlling both friction and alloy transfer to SiC during multipass slidings.

Crystallographic orientation (anisotropy) effects.—Metals and ceramics exhibit anisotropic behavior in many of their mechanical properties. The friction and wear behaviors of ceramics are also anisotropic under adhesive conditions.

Anisotropy results can be of two kinds:

1. The observed variation in friction and wear when the sliding surface is changed from one crystal plane to another for a given material

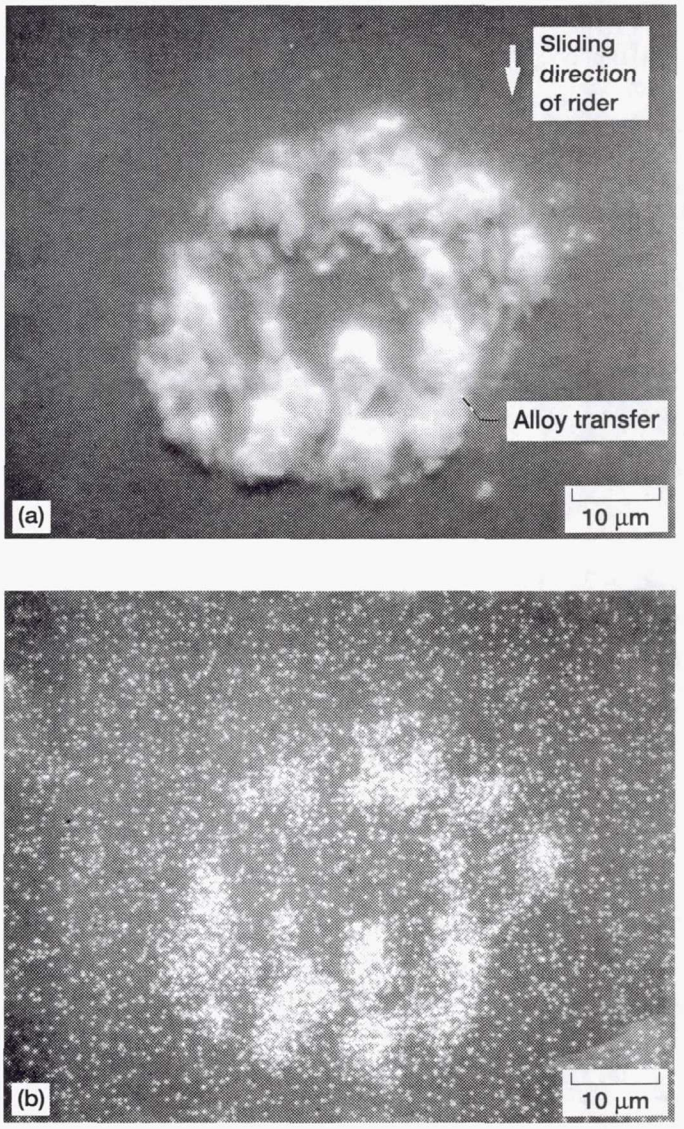

Figure 3.18.—Transfer of titanium-iron binary alloy (8.12-at.% Ti) to single-crystal SiC {0001} surface at start of sliding. Sliding direction, $\langle 1\bar{0}10 \rangle$; sliding velocity, 3 mm/min; load, 0.2 N; room temperature; vacuum pressure, 10^{-8} Pa.

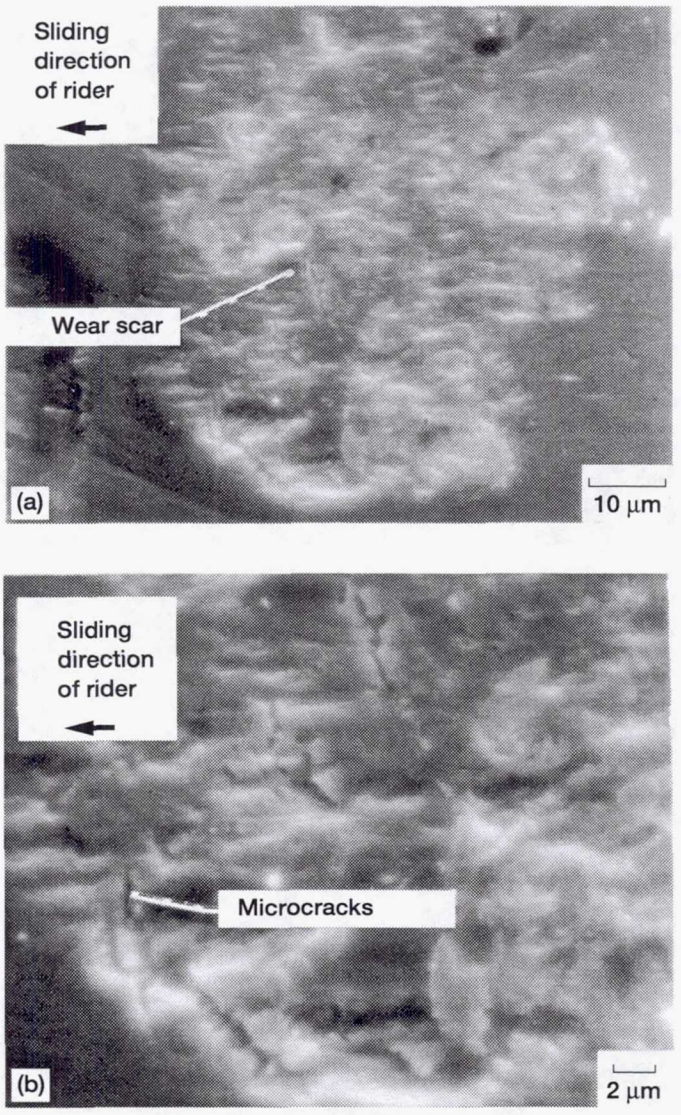

Figure 3.19.—Wear scar on titanium-iron binary alloy (8.12-at.% Ti) showing grooves and cracks after single-pass sliding on single-crystal SiC {0001} surface. Sliding direction, $\langle 10\bar{1}0 \rangle$; sliding velocity, 3 mm/min; load, 0.2 N; room temperature; vacuum pressure, 10^{-8} Pa.

2. The variation in friction and wear observed when the orientation of the sliding surface is changed with respect to a specific crystallographic direction on a given crystal plane

For example, the differences in the coefficients of friction with respect to the mating crystallographic planes and directions are significant under adhesive conditions, as indicated in Table 3.6 (from [3.68]). The data of Table 3.6 were obtained in vacuum with clean ferrite–ferrite oxide ceramics. The mating of preferred slip plane with highest atomic density plane and direction, such as $\{110\}\langle 110\rangle$ and $\{111\}\langle 110\rangle$ for Mn-Zn ferrite, gave the lowest coefficients of friction. In other words, the lowest coefficients of friction were obtained on the preferred slip plane when sliding in the preferred slip direction. Similar results have been obtained with SiC and Al_2O_3 (sapphire). Table 3.7 shows their anisotropic friction. Again, the coefficients of friction were lowest on the preferred basal slip plane when sliding in the preferred $\langle 11\bar{2}0\rangle$ slip direction [3.69, 3.70]. The coefficient of friction reflects the force required to shear at the interface when the SiC or Al_2O_3 basal planes are parallel to the interface. The results presented in Table 3.7 indicate that lower force is required to resist shear fracture of the adhesive bond at the interface in the preferred crystallographic $\langle 11\bar{2}0\rangle$ direction than in the $\langle 10\bar{1}0\rangle$ direction.

When the SiC $\{0001\}$ surface was in contact with iron, as shown in Fig. 3.20, from room temperature to 800 °C in vacuum, the coefficient of friction was lower in the $\langle 11\bar{2}0\rangle$ direction than in the $\langle 10\bar{1}0\rangle$ direction over the entire temperature range [3.69]. The coefficient of friction generally increased with increasing temperature from about 0.5 in the $\langle 10\bar{1}0\rangle$ sliding direction and 0.4 in the $\langle 11\bar{2}0\rangle$ sliding direction at room temperature to 0.75 and 0.63, respectively, at about 800 °C. Although the coefficient of friction remained low below 300 °C, it increased rapidly with increasing temperature from 300 to 600 °C. There was, however, little further increase in friction above 600 °C.

TABLE 3.6.—ANISOTROPIC FRICTION FOR Mn-Zn FERRITE *CONTACTING SiC UNDER ADHESIVE CONDITIONS*

[Load, 0.05 to 0.5 N; sliding velocity, 3 mm/min; vacuum pressure, 10^{-8} Pa; room temperature.]

Mated plane	Mated direction	Sliding direction	Coefficient of friction
Effect of crystallographic plane			
{110} on {110}	⟨110⟩on ⟨110⟩	⟨110⟩	0.21
{111} on {111}	⟨110⟩on ⟨110⟩	⟨110⟩	.21
{100} on {100}	⟨110⟩on ⟨110⟩	⟨110⟩	.24
{110} on {100}	⟨110⟩on ⟨110⟩	⟨110⟩	.27
{110} on {111}	⟨110⟩on ⟨110⟩	⟨110⟩	.29
{110} on {211}	⟨110⟩on ⟨110⟩	⟨110⟩	.29
Effect of crystallographic direction			
{110} on {110}	⟨110⟩on ⟨110⟩	⟨110⟩	0.21
	⟨110⟩on ⟨100⟩	⟨110⟩	.43

TABLE 3.7.—ANISOTROPIC FRICTION FOR SAPPHIRE AND SiC CONTACTING THEMSELVES UNDER ADHESIVE CONDITIONS

Plane	Direction	Coefficient of friction
Sapphire sliding on sapphire[a]		
Prismatic {1010}	$\langle 11\bar{2}0 \rangle$	0.93
	$\langle 0001 \rangle$	1.00
Basal {0001}	$\langle 11\bar{2}0 \rangle$	0.50
	$\langle 10\bar{1}0 \rangle$	.96
SiC sliding on SiC[b]		
Basel {0001}	$\langle 1120 \rangle$	0.54
	$\langle 10\bar{1}0 \rangle$	.68

[a]Load, 10 N; sliding velocity, 7.8 mm/min; vacuum pressure, 10^{-8}; room temperature.
[b]Load, 0.3 N; sliding velocity, 3 mm/min; vacuum pressure, 10^{-8} Pa; room temperature.

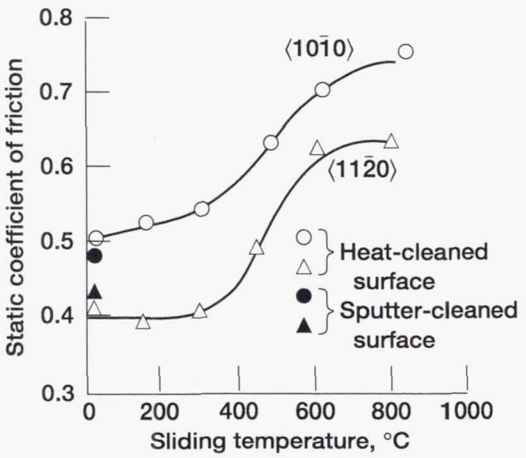

Figure 3.20.—Static coefficient of friction as function of sliding temperature and crystallographic orientation for SiC surface sliding against iron. Normal load, 0.2 N; vacuum pressure, 10^{-8} Pa. (The surfaces were heat cleaned at 800 °C before the friction experiments. The coefficient of friction was obtained by averaging three to five measurements.)

The data of Fig. 3.20 indicate that the friction behavior of SiC in contact with iron is highly anisotropic over the entire range from room temperature to 800 °C. Several slip systems have been observed in α-SiC, including the $\{0001\}\langle 11\bar{2}0\rangle$, $\{3\bar{3}01\}\{11\bar{2}0\}$, and $\langle 10\bar{1}0\rangle\{11\bar{2}0\}$ systems [3.69, 3.71]. The preferred crystallographic slip direction, or the shear direction for the basal $\{0001\}$ plane, is the $\langle 11\bar{2}0\rangle$ direction. The coefficient of friction on the basal plane was lower in the $\langle 11\bar{2}0\rangle$ direction than in the $\langle 10\bar{1}0\rangle$ direction.

The coefficient of friction reflects the force required to shear at the interface when the SiC basal planes are parallel to the interface. The results presented in Fig. 3.20 indicate that less force is required to resist shear fracture of the adhesive bond at the interface in the $\{11\bar{2}0\}$ direction than in the $\langle 10\bar{1}0\rangle$ direction.

SiC $\{0001\}$ surfaces that were argon sputter cleaned or heat cleaned in situ revealed no significant differences in coefficient of friction. The frictional anisotropy was also similar (i.e., the coefficient of friction was lower in the $\langle 11\bar{2}0\rangle$ direction than in the $\langle 10\bar{1}0\rangle$ direction).

Sliding a metal or SiC pin on an SiC flat $\{0001\}$ surface resulted in cracks along cleavage planes of $\langle 10\bar{1}0\rangle$ orientation. Figure 3.21 shows scanning electron micrographs of the wear tracks generated by 10 passes of rhodium and titanium pins on the SiC $\{0001\}$ surface along the $\langle 10\bar{1}0\rangle$ direction. The cracks observed in the wear tracks propagated primarily along cleavage planes of the $\langle 10\bar{1}0\rangle$ orientation. Figure 3.21(a) reveals a hexagonal light area, which is the beginning of a wear track, and a large crack. Cracks were generated primarily along the $\langle 10\bar{1}0\rangle$ planes, propagated, and then intersected during loading and sliding of the rhodium pin over the SiC surface. It is anticipated from Fig. 3.21(a) that substrate cleavage cracking of the $\{0001\}$ planes, which are parallel to the sliding surface, also occurs. Figure 3.21(b) reveals a hexagonal pit surrounded by a copious amount of thin titanium film. The hexagonal fracturing is caused primarily by cleavage cracking along the $\langle 10\bar{1}0\rangle$ planes and subsurface cleavage cracking along the $\{0001\}$ planes. The smooth surface at the bottom of the hexagonal pit is due to cleavage of the $\{0001\}$ planes.

Figure 3.22 illustrates the SiC wear debris produced by 10-pass sliding of aluminum pins on an SiC surface. The scanning electron micrographs reveal evidence of multiangular SiC wear debris particles with transferred aluminum wear debris on the SiC wear track. These multiangular wear debris particles had crystallographically oriented sharp edges and were nearly hexagonal, rhombic, parallelogramic, or square [3.71]. These shapes may be related to surface and subsurface cleavage of $\langle 10\bar{1}0\rangle$, $\langle 11\bar{2}0\rangle$, and $\{0001\}$ planes.

Similar hexagonal pits and multiangular wear debris with crystallographically oriented sharp edges were also observed with single-crystal SiC in contact with itself. Figure 3.23 clearly reveals the gross hexagonal pits on the wear scar of the SiC pin and a nearly fully hexagonal and flat wear particle. The wear debris had transferred to the flat SiC specimen. Thus, crystallographically oriented cracking and fracturing of SiC resulted from both sliding of the metal pin and sliding of the SiC pin.

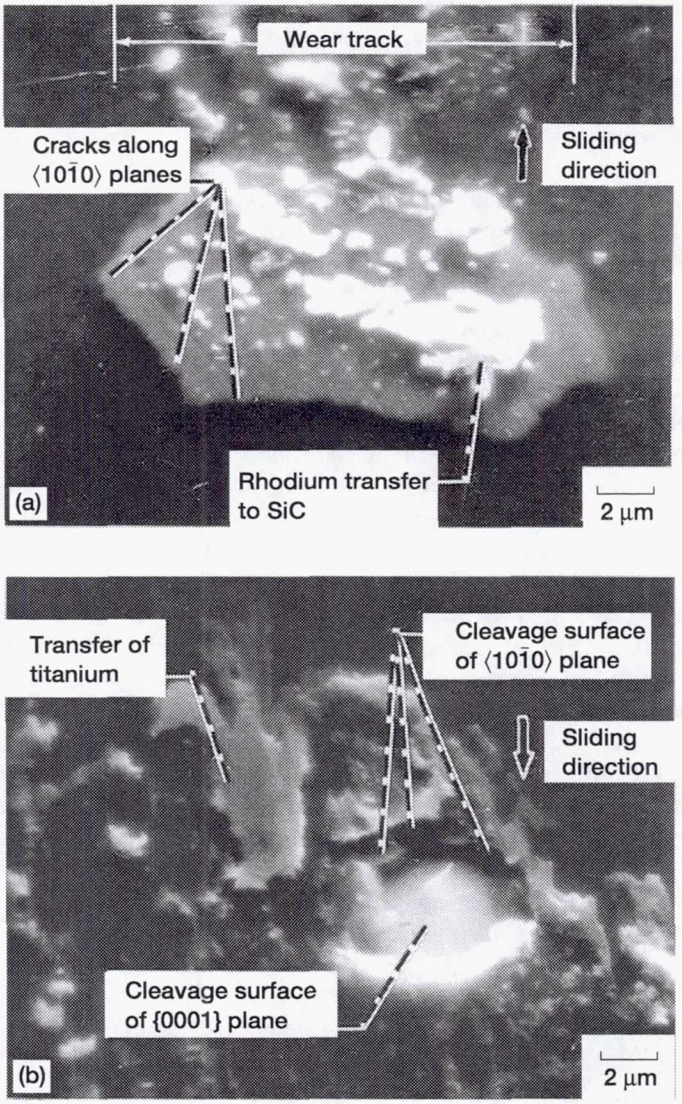

Figure 3.21.—Scanning electron micrographs of wear tracks on single-crystal SiC {0001} surface after 10 passes of rhodium and titanium pins in vacuum. Sliding direction, ⟨10$\bar{1}$0⟩; sliding velocity, 3 mm/min; load, 0.3 N; room temperature; vacuum pressure, 10^{-8} Pa. (a) Rhodium pin; hexagonal cracking. (b) Titanium pin; hexagonal pit.

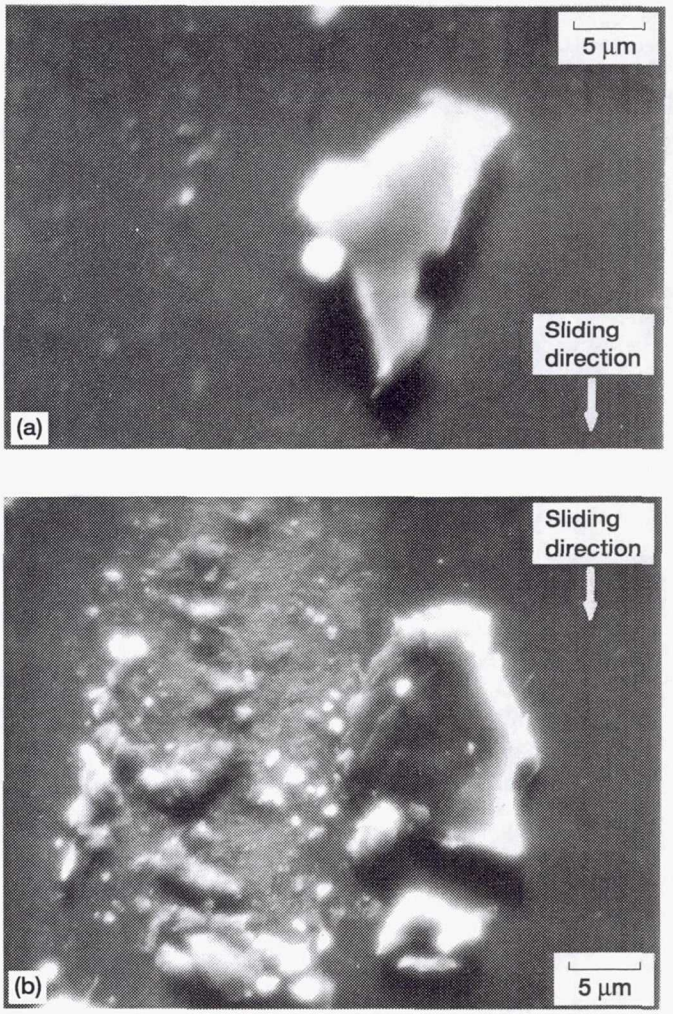

Figure 3.22.—Scanning electron micrographs of wear tracks on and multiangular wear debris of flat single-crystal SiC {0001} surface after 10 passes of aluminum pin in vacuum. Sliding direction, $\langle 10\bar{1}0 \rangle$; sliding velocity, 3 mm/min; load, 0.2 N; room temperature; vacuum pressure, 10^{-8} Pa.

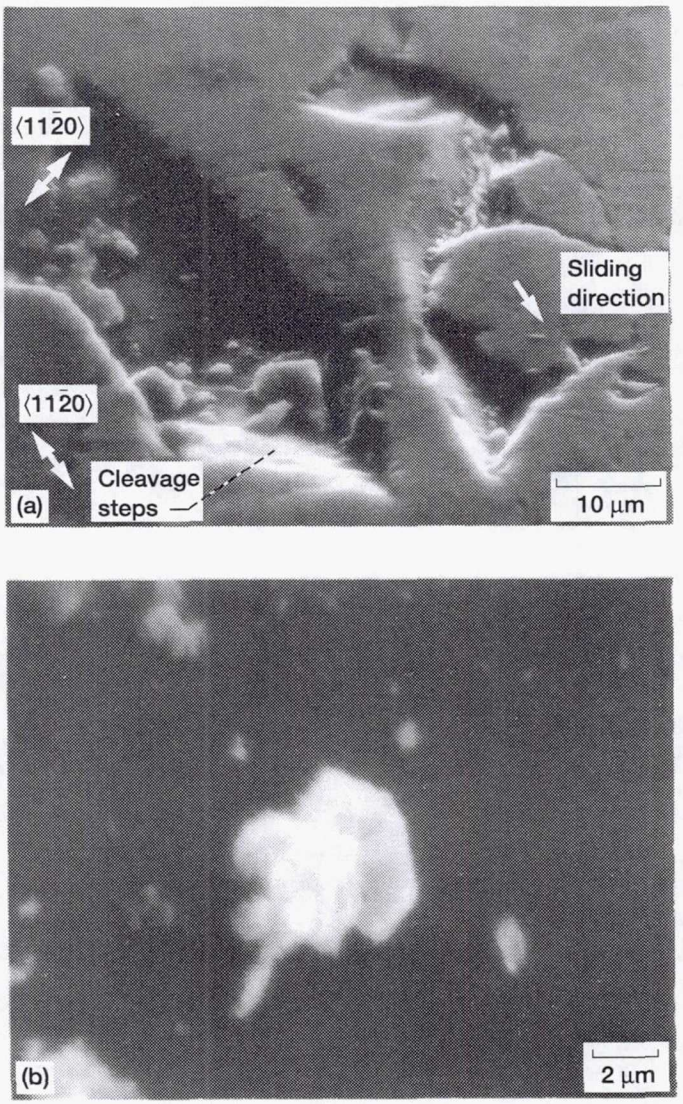

Figure 3.23.—Scanning electron micrographs of wear debris on single-crystal SiC {0001} surface after 10 passes of SiC pin in vacuum. Sliding direction, ⟨10$\bar{1}$0⟩; sliding velocity, 3 mm/min; load, 0.5 N; room temperature; vacuum pressure, 10^{-8} Pa.

In summary, it has been shown that the friction and wear characteristics of single crystals are anisotropic. In general, the lowest coefficient of friction was observed when sliding was in the preferred slip direction on the preferred slip plane. Wear and fracture due to adhesion of clean surfaces behave with respect to crystallographic orientation in the same way as does friction.

3.6 Friction Mechanism of Clean, Smooth Surfaces

All the clean metal-ceramic couples, including the metal-diamond couples, exhibited a correlation between the surface and bulk properties of the metal (e.g., its Young's and shear moduli, its bond strength, and the chemistry of the contacting materials) and the adhesion, friction, and wear behaviors of the metal. All the following properties decreased as the metal's elastic (Young's) and shear moduli increased or its chemical activity decreased: adhesion, coefficient of friction, metal wear, and metal transfer to the ceramic. Perhaps the metal's bulk properties depend on the magnitude of its surface properties. It is interesting to consider then the role that the metal's basic surface and bulk properties, as found in the literature (such as its surface energy per unit area γ and its ductility) play in the adhesion, friction, wear, and transfer of metal-ceramic couples.

The surface energy per unit area γ of a metal is directly related to the interfacial bond strength per unit area at the metal-ceramic interface [3.61]. Figure 3.24 presents the γ values suggested by Tyson [3.48] and Miedema [3.56] for various metals at room temperature as a function of the shear modulus of the metal. As γ increased, so did the shear modulus. A comparison with Figs. 3.5(a) and 3.15(a)

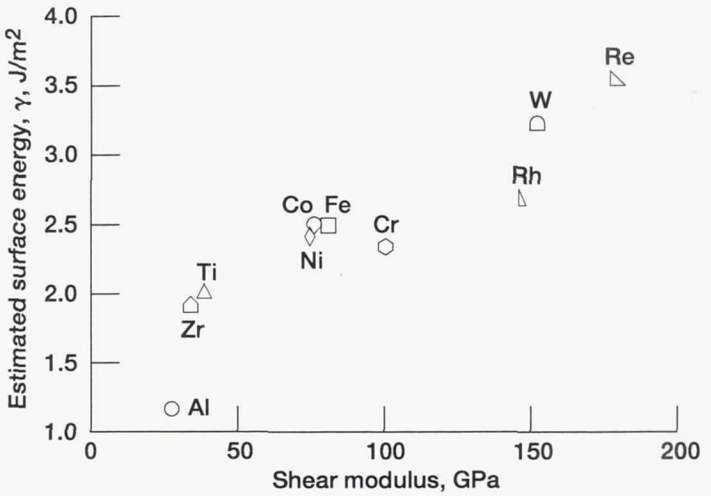

Figure 3.24.—Estimated surface energy as function of shear modulus for various metals.

shows that γ (the surface or bond energy) behaved in the opposite manner from the coefficient or friction, which decreased with an increase in γ. Obviously, γ alone does not explain the friction trend shown in Figs. 3.5(a) and 3.15(a). Certainly, if γ is low, the interfacial bond strength per unit area is weak, but that does not mean that a low interfacial bond strength per unit area gives a mechanically weak interface in the real area of contact between the metal and ceramic surfaces.

A metal's ductility influences the real area of contact and accordingly the adhesion and friction at the metal-ceramic interface. Ceramics such as Si_3N_4 and SiC, unlike metals, are not considered to be ductile; these materials behave in a ductile manner only when subjected to high compressive stresses. Because of the marked difference in the ductilities of ceramics and metals, solid-state contact between the two materials can result in considerable plastic deformation of the softer metal. The real area of contact then for such a couple must be calculated from the experimentally measured Vickers hardness of the metal. In this calculation the yield pressure of the surface asperities on the metal is assumed to be approximately the same as that of the bulk metal. Furthermore, no consideration is given to the growth of the real area of contact, known as junction growth, under both normal and shear (tangential) stresses acting at the interface. The real area of contact A is simply determined from the ratio of normal load to hardness. The hardness data were obtained from micro-Vickers indentation measurements of wear scars on metal pin specimens at a load of 0.25 N in an air environment. The calculated value of A depended strongly on the shear modulus of the metal (Fig. 3.25), decreasing as the shear modulus of the metal increased. The real area of contact obviously behaves in the same way as the coefficient of friction (see Figs. 3.5(a), 3.15(a), and 3.25).

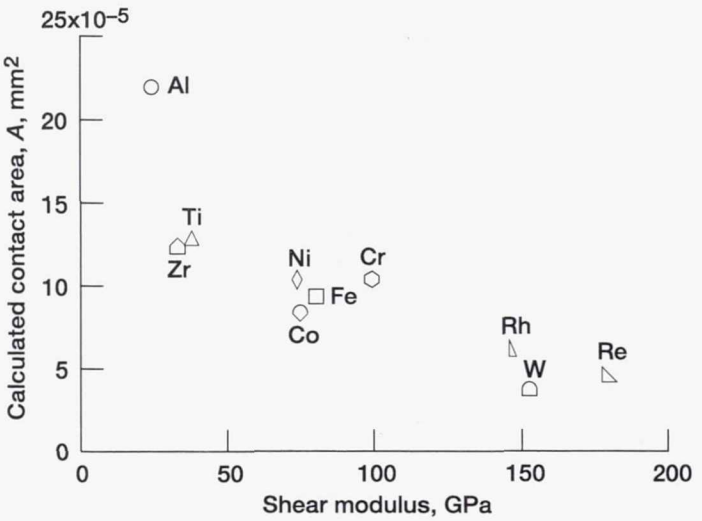

Figure 3.25.—Calculated contact area as function of shear modulus for various metals.

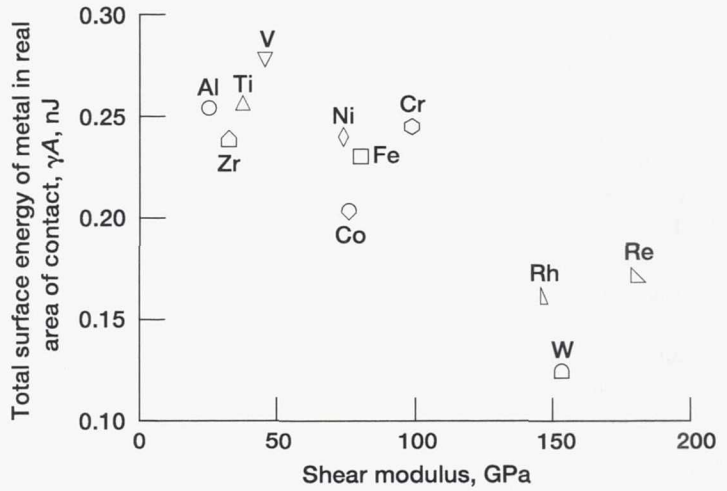

Figure 3.26.—Total surface energy in real area of contact as function of shear modulus for various metals.

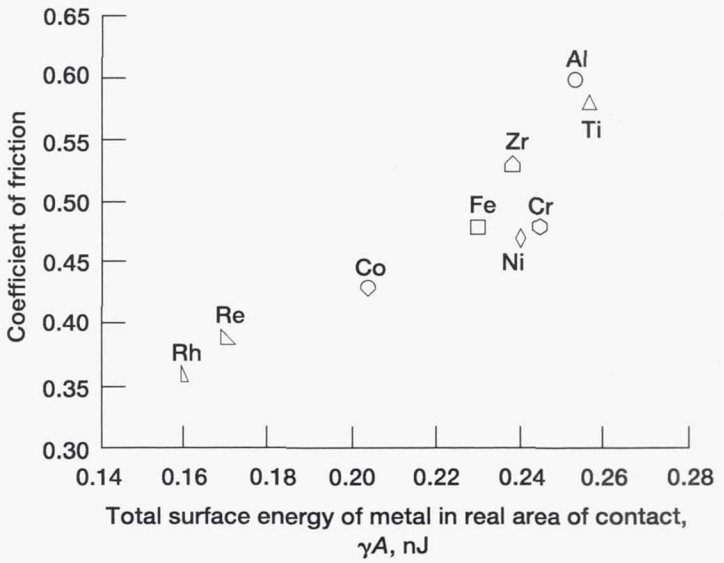

Figure 3.27.—Coefficient of friction for various metals in sliding contact with SiC {0001} surface in ultrahigh vacuum as function of total surface energy of metal in real area of contact.

A metal's total surface energy in the real area of contact is the product of the surface energy per unit area γ and the real area of contact A. It too decreased as the shear modulus of the metal increased. This relationship is brought out clearly in Fig. 3.26, which shows γA plotted against the shear modulus of the metal.

Comparing Fig. 3.26 with Figs. 3.5(a) and 3.15(a) shows that γA is associated with tribological behavior; the higher the value of γA, the greater the adhesion and friction. In addition, Fig. 3.27 clearly shows that the coefficient of friction for metal-SiC {0001} couples increased as γA increased. Comparing Table 3.2 with Fig. 3.26 indicates that γA is also related to metal wear and transfer to the ceramic (i.e., SiC); the higher the value of γA, the greater the metal wear and transfer.

The evidence from the adhesion and friction experiments reported herein points to the establishment of strong interfacial bonds in the real area of contact when clean metal-ceramic surfaces are brought into contact.

3.7 Concluding Remarks

When a clean metal was brought into contact with a clean, harder ceramic in ultrahigh vacuum, strong bonds were formed between the two materials. The coefficient of friction for clean surfaces of metal-ceramic couples, which reflects interfacial adhesion, was found to correlate with the metal's total surface energy γ in the real area of contact A (i.e., the product γA). The coefficient of friction increased as the metal's total surface energy increased.

The interfacial bond between metal and ceramic surfaces was generally stronger than the cohesive bond in the metal. Thus, the metal fractured when shear occurred. The observed metal wear and transfer to the ceramic were mainly caused by the strength of the interfacial bonds and the shear fracture of the metal. The metal's total surface energy in the real area of contact was also associated with its wear and transfer at the metal-ceramic interface. The higher the metal's total surface energy, the greater its wear and transfer.

All the following properties are related to the Young's and shear moduli of the metal: adhesion, coefficient of friction, metal wear and transfer, the metal's surface energy per unit area, the real area of contact calculated from hardness, and the metal's total surface energy in the real area of contact. With the exception of surface energy per unit area, all decreased as the Young's and shear moduli of the metal increased. Only the surface energy (i.e., bond energy) per unit area of the metal increased when the Young's and shear moduli increased.

As a practical matter, an understanding of how clean surfaces of metal-ceramic couples behave is relevant to the problem of forming strong bonds between metal and ceramic surfaces and to the friction and wear properties of the materials.

References

3.1 D.H. Buckley, *Surface Effects in Adhesion, Friction, Wear and Lubrication*, Elsevier Book Series, Elsevier Scientific Publishing Co., Vol. 5, 1981.

3.2 D.H. Buckley, The use of analytical surface tools in the fundamental study of wear, *Wear 46,1*: 19–53 (1978).

3.3 D. Tabor, Status and direction of tribology as a science in the 80's—understanding and prediction, *New Directions in Lubrication, Materials, Wear, and Surface Interactions* (W.R. Loomis, ed.), Noyes Publications, Park Ridge, NJ, Vol. 1, 1985, pp. 1–17. (Also NASA CP–2300.)

3.4 K. Miyoshi and D.H. Buckley, Considerations in friction and wear, *New Directions in Lubrication, Materials, Wear, and Surface Interactions* (W.R. Loomis, ed.), Noyes Publications, Park Ridge, NJ, Vol. 1, 1985, pp. 291–320. (Also NASA CP–2300.)

3.5 K. Miyoshi and D.H. Buckley, Surface chemistry and wear behavior of single-crystal silicon carbide sliding against iron at temperatures to 1500 °C in vacuum, NASA TP–1947 (1982).

3.6 D. Tabor, *The Properties of Diamond* (J.E. Field, ed.), Academic Press, New York, 1979, pp. 325–350.

3.7 K. Miyoshi, Uses of Auger and x-ray photoelectron spectroscopy in the study of adhesion and friction, *Advances in Engineering Tribology, Proceedings of the First International Symposium on Industrial Tribology* (Y.-W. Chung and H.S. Cheng, eds.), STLE SP–31, Society of Tribologists and Lubrication Engineers, 1991, pp. 3–12.

3.8 K. Miyoshi, Uses of AES and XPS in adhesion, friction, and wear studies, *Surface Diagnostics in Tribology* (K. Miyoshi and Y-W. Chung, eds.), World Scientific Publishing Co., Inc., Vol. 1, 1993, pp. 93–134.

3.9 K. Miyoshi and D.H. Buckley, Properties of ferrites important to their friction and wear behavior, *Tribology and Mechanics of Magnetic Storage Systems* (Including the Symposium Proceedings of the Annual ASME–ASLE Lubrication Conference) (B. Bhushan, ed.), ASLE SP–16, American Society of Lubrication Engineers, 1984, pp. 13–20.

3.10 K. Miyoshi, C. Maeda, and R. Masuo, Development of a torsion balance for adhesion measurements, *Instrumentation for the 21st Century* (Including the Proceedings of the 11th Triennial World Congress of the International Measurement Confederation (IMEKO XI)), Instrument Society of America, 1988, pp. 233–248.

3.11 K. Miyoshi, Design, development, and applications of novel techniques for studying surface mechanical properties, *Interfaces Between Polymers, Metals, and Ceramics* (Including the Proceedings of the Materials Research Society Symposium), Materials Research Society, Vol. 153,1989, pp. 321–330.

3.12 J.M. Georges, ed., *Microscopic Aspects of Adhesion and Lubrication: Proceedings of the 34th International Meeting of the Societe de Chimie Physique*, Elsevier Scientific Publishing Co., 1982.

3.13 H. Czichos, *Tribology—A Systems Approach to the Science and Technology of Friction, Lubrication and Wear*, Elsevier Scientific Publishing Co., 1978.

3.14 J. Ferrante and J.R. Smith, A theory of adhesion at a bimetallic interface: overlap effects, *Surf. Sci. 38*: 77–92 (1973).

3.15 D.V. Keller, Jr., and R.G. Aldrich, Adhesion of metallic bodies initiated by physical contact, *J. Adhesion 1, 2*: 142–156 (1969).

3.16 J.B. Pethica and D. Tabor, Contact of characterized metal surfaces at very low loads: deformation and adhesion, *Surf. Sci. 89*: 182–190 (1979).

3.17 M.D. Pashley and D. Tabor, Adhesion and deformation properties of clean and characterized metal micro-contacts, *Vacua 31, 10–12*: 619–623 (1981).

3.18 J.E. Ingelsfield, Adhesion between Al slabs and mechanical properties, *J. Phys. F. Met. Phys. 6, 5*: 687–701 (1976).

3.19 D.D. Eley, *Adhesion*, Oxford University Press, London, 1961.

3.20 G.A.D. Briggs and B.J. Briscoe, Surface roughness and the friction and adhesion of elastomers, *Wear 57,* 2: 269–280 (1979).
3.21 N. Gane, P.F. Pfaelzer, and D. Tabor, Adhesion between clean surfaces at light loads, *Proc. R. Soc. London A340, 1623*: 495–517 (1974).
3.22 N.T. Saunders, Impact and promise of NASA aeropropulsion technology, *Aeropropulsion 1987*, NASA CP–10003, Vol. 1, 1988, pp. 1–30.
3.23 S.J. Grisaffe, Lewis materials research and technology: an overview, *Aeropropulsion 1987*, NASA CP–10003, Vol. 1, 1988, pp. 31–38.
3.24 M.A. Meador, High temperature polymer matrix composites, *Aeropropulsion1987*, NASA CP–10003, Vol. 1, 1988, pp. 39–53.
3.25 J. Gayda, Creep and fatigue research efforts on advanced materials, *Aeropropulsion 1987*, NASA CP–10003, Vol. 1, 1988, pp. 55–72.
3.26 P.K. Brindley, Development of a new generation of high-temperature composite materials, *Aeropropulsion 1987*, NASA CP–10003, Vol. 1, 1988, pp. 73–87.
3.27 J.D. Kiser, S.R. Levine, and J.A. DiCarlo, Ceramics for engines, *Aeropropulsion 1987*, NASA CP–10003, Vol. 1, 1988, pp. 103–120.
3.28 W.E. Hazen and R.W. Pidd, *Physics*, Addison-Wesley Publishing Co., Reading, MA, 1965.
3.29 F.W. Sears and M.W. Zemansky, *College Physics—Mechanics, Heat, and Sound*, Second ed., Addison-Wesley Press Inc., Cambridge, MA, 1952.
3.30 S.V. Pepper, Shear strength of metal-sapphire contacts, *J. Appl. Phys. 47*:801–808 (1976).
3.31. K.A. Gschneidner, Jr., Physical properties and interrelationships of metallic and semimetallic elements, *Solid State Physics, Advances* in *Research Applications* (F. Seitz and D. Turnbull, eds.), Academic Press, Vol. 16, 1964, pp. 275–426.
3.32 A.R. Von Hippel, *Dielectrics and Waves*, John Wiley & Sons, Inc., New York, 1954, pp. 219–228.
3.33 W.D. Kingery, H.K. Bowen, and D.R. Uhlmann, *Introduction to Ceramics*, Second ed., John Wiley & Sons, Inc., 1976, pp. 25–88, 975–1015.
3.34 A.Y. Liu and M.L. Cohen, Prediction of new low compressibility solids, *Science 245*: 841–842 (1989).
3.35 A.Y. Liu and M.L. Cohen, Structural properties and electronic structure of low-compressibility materials: β-Si_3N_4 and hypothetical β-C_3N_4, *Phys. Rev. B 41, 15*: 10727–10734 (1990).
3.36 K. Miyoshi and D.H. Buckley, Friction and wear of single-crystal manganese-zinc ferrite, *Wear 66, 2*: 157–173 (1981).
3.37 K. Miyoshi and D.H. Buckley, Adhesion and friction of single-crystal diamond in contact with transition metals, *Appl. Surf. Sci. 6, 2*: 161–172 (1980).
3.38 K. Miyoshi and D.H. Buckley, Friction and wear behavior of single-crystal silicon carbide in sliding contact with various metals, *ASLE Trans. 22, 3*: 245–256 (1979).
3.39 D.H. Buckley, The metal-to-metal interface and its effect on adhesion and friction, *J. Colloid Interface Sci. 58, 1*: 36–53 (1977).
3.40 D.H. Buckley, Friction and transfer behavior of pyrolytic boron nitride in contact with various metals, *ASLE Trans. 21, 2*: 118–124 (1978).
3.41 K. Miyoshi and D.H. Buckley, Correlation of tensile and shear strengths of metals with their friction properties, *ASLE Trans. 27, 1*: 15–23 (1984).
3.42 N.H. Macmillan, Review: the theoretical strength of solids, *J. Mater. Sci. 7, 2*: 239–254 (1972).
3.43 M. Polanyi, Uber die Natur des zerrei Bvorganges, *Z. Physik 7*: 323–327 (1921).
3.44 E. Orowan, Mechanical cohesion properties and the "real" structure of crystals, *Z. Kristallog, Kristallgeom, Kristallphys, Kristallchem 89*:327–343 (Oct. 1934).
3.45 E. Orowan, Fracture and strength of solids, *Rep. Phys. Soc. Prog. Phys. 12*: 185–232 (1948–49).
3.46 E. Orowan, Energy criteria of fracture, *Weld J. 34, 3*: 157S–160S (1955).
3.47 J. Frenkel, Zur Theorie der Elastizitatsgrenze and der festigkeit kristallinischer Korper, *Z. Phys. 37*: 572–609 (1926).
3.48 W.R. Tyson, Surface energies of solid metals, *Can. Metall. Q. 14, 4*:307–314 (1975).

3.49 H. Jones, The surface energy of solid metals, *Met. Sci. J. 5*: 15–18 (1971).
3.50 L.E. Murr, *Interfacial Phenomena in Metals and Alloys*, Addison-Wesley Publishing Co., Reading, MA, 1975.
3.51 S.H. Overbury, P.A. Bertrand, and G.A. Somorjai, Surface composition of binary systems: prediction of surface phase diagrams of solid solutions, *Chem. Rev. 75, 5*: 547–560 (1975).
3.52 N. Eustathopoulos, J.C. Joud, and P. Desre, Interfacial tension of pure metals, Part I—Estimation of the liquid-vapor and solid-vapor surface tensions from the cohesion energy, *J. Chim. Phys.—Phys. Chim. Biol. 70, 1*: 42–48 (1973).
3.53 N. Eustathopoulos, J.C. Joud, and P. Desre, Interfacial tension of pure metals, Part II—Estimation of the solid-vapor and solid-liquid interfacial tensions from the surface tension of liquid metals, *J. Chim. Phys.—Phys. Chim. Biol. 70, 1*: 49–53 (1973).
3.54 R.G. Linford, Surface thermodynamics of solids, *Solid State Surface Science II* (M. Green, ed.), Marcel Dekker, 1973, pp. 1–152.
3.55 T.A. Roth, Surface and grain-boundary energies of iron, cobalt, and nickel, *Mater. Sci. Eng. 18, 2*: 183–192 (1975).
3.56 A.R. Miedema, Surface energies of solid metals, *Z. Metallk. 69, 5*: 287–292 (1978).
3.57 P.W. Bridgman, Shearing phenomena at high pressures, particularly in inorganic compounds, *Proc. Am. Acad. Arts Sci. 71*: 387–459 (1937).
3.58 S. Timoshenko and J.N. Goodier, *Theory of Elasticity*, Second ed., McGraw-Hill Book Co., New York, 1951.
3.59 D. Landau, Hardness: A Critical Examination of Hardness, Dynamic Hardness, and an Attempt To Reduce Hardness to Dimensional Analysis, The Nitralloy Corporation, New York, 1943.
3.60 D. Tabor, *The Hardness of Metals*, Clarendon Press, Oxford, 1951.
3.61 E. Rabinowicz, *Friction and Wear of Materials*, John Wiley & Sons, Inc., New York, 1965.
3.62 D.H. Buckley, *Friction, Wear, and Lubrication in Vacuum*, NASA SP–277, 1971.
3.63 L. Pauling, A resonating-valence-bond theory of metals and intermetallic compounds, *Proc. R. Soc. London A196*: 343–362 (1949).
3.64 W. Hayden, W.G. Moffatt, and J. Wulff, Mechanical Behavior, *The Structure and Properties of Materials*, John Wiley & Sons, Inc., New York, Vol. 3, 1965.
3.65 K. Miyoshi and D.H. Buckley, The adhesion, friction, and wear of binary alloys in contact with single-crystal silicon carbide, *J. Lubr. Technol. 103*: 180–187 (1981).
3.66 K. Miyoshi and D.H. Buckley, The friction and wear of metals and binary alloys in contact with an abrasive grit of single-crystal silicon carbide, *ASLE Trans. 23, 4*: 460–477 (1980).
3.67 J.R. Stephens and W.R. Witzke, Alloy softening in binary iron solid solutions, *J. Less Common Met. 48*: 285–308 (Aug. 1976).
3.68 D.H. Buckley and K. Miyoshi, Tribological properties of structural ceramics, *Treatise on Materials Science and Technology* (John B. Wachtman, Jr., ed.), Academic Press, Inc., Boston, 1989, pp. 293–365.
3.69 K. Miyoshi and D.H. Buckley, Anisotropic tribological properties of SiC, *Wear 75, 2*: 253–268 (1982).
3.70 D.H. Buckley, Friction and wear behavior of glasses and ceramics, *Mater. Sci. Res. 7*: 101–126 (1974).
3.71 K. Miyoshi and D.H. Buckley, Wear particles of single-crystal silicon carbide in vacuum, NASA TP–1624 (1980).

REPORT DOCUMENTATION PAGE

Form Approved
OMB No. 0704-0188

Public reporting burden for this collection of information is estimated to average 1 hour per response, including the time for reviewing instructions, searching existing data sources, gathering and maintaining the data needed, and completing and reviewing the collection of information. Send comments regarding this burden estimate or any other aspect of this collection of information, including suggestions for reducing this burden, to Washington Headquarters Services, Directorate for Information Operations and Reports, 1215 Jefferson Davis Highway, Suite 1204, Arlington, VA 22202-4302, and to the Office of Management and Budget, Paperwork Reduction Project (0704-0188), Washington, DC 20503.

1. AGENCY USE ONLY (*Leave blank*)	2. REPORT DATE	3. REPORT TYPE AND DATES COVERED
	July 1998	Technical Memorandum

4. TITLE AND SUBTITLE

Solid Lubrication Fundamentals and Applications
Properties of Clean Surfaces: Adhesion, Friction, and Wear

5. FUNDING NUMBERS

WU–505–63–5A

6. AUTHOR(S)

Kazuhisa Miyoshi

7. PERFORMING ORGANIZATION NAME(S) AND ADDRESS(ES)

National Aeronautics and Space Administration
Lewis Research Center
Cleveland, Ohio 44135–3191

8. PERFORMING ORGANIZATION REPORT NUMBER

E–9863–3

9. SPONSORING/MONITORING AGENCY NAME(S) AND ADDRESS(ES)

National Aeronautics and Space Administration
Washington, DC 20546–0001

10. SPONSORING/MONITORING AGENCY REPORT NUMBER

NASA TM—1998-107249
CH3

11. SUPPLEMENTARY NOTES

Responsible person, Kazuhisa Miyoshi, organization code 5140, (216) 433–6078.

12a. DISTRIBUTION/AVAILABILITY STATEMENT

Unclassified - Unlimited
Subject Category: 27 Distribution: Nonstandard

This publication is available from the NASA Center for AeroSpace Information, (301) 621–0390.

12b. DISTRIBUTION CODE

13. ABSTRACT ***(Maximum 200 words)***

This chapter presents the adhesion, friction, and wear behaviors of smooth, atomically clean surfaces of solid-solid couples, such as metal-ceramic couples, in a clean environment. Surface and bulk properties, which determine the adhesion, friction, and wear behaviors of solid-solid couples, are described. The primary emphasis is on the nature and character of the metal, especially its surface energy and ductility. Also, the mechanisms of friction and wear for clean, smooth surfaces are stated.

14. SUBJECT TERMS

Solid lubrication; Coatings; Tribology fundamentals; Applications

15. NUMBER OF PAGES

53

16. PRICE CODE

A04

17. SECURITY CLASSIFICATION OF REPORT	18. SECURITY CLASSIFICATION OF THIS PAGE	19. SECURITY CLASSIFICATION OF ABSTRACT	20. LIMITATION OF ABSTRACT
Unclassified	Unclassified	Unclassified	